J. Fluid Mech. (1981), *vol.* 104, *pp.* 1–43
Printed in Great Britain

Structure of space–time correlations of bursting phenomena in an open-channel flow

By HIROJI NAKAGAWA AND IEHISA NEZU
Department of Civil Engineering, Kyoto University, Kyoto 606, Japan

(Received 8 October 1979 and in revised form 14 March 1980)

The present study is to investigate the structure of space–time correlations of bursting motions, such as ejections and sweeps in an open-channel flow, by a new conditional sampling analysis of the instantaneous velocity and Reynolds-stress signals measured simultaneously by two dual-sensor hot-film probes. One probe was fixed near the edge of the buffer layer, while the other probe was moved in the streamwise, vertical and spanwise directions. The sorted instantaneous Reynolds-stress signals obtained from the fixed probe were used as a detecting information of the occurrences of ejection or sweep events. The streamwise and vertical spatial characteristics of the ejection–sweep motions, and their convection process are investigated in detail. Also, the spanwise spatial properties of the high- and low-speed streaks in the bursting motions are examined experimentally by the present conditional sampling method.

Next, a qualitative model is proposed which attempts to explain the space–time structures of the bursting phenomenon, on the basis of the above anemometry information and other visual observations.

1. Introduction

In the past ten years intensive experimental research on the turbulence-production mechanism and the bursting phenomenon over a smooth solid bed has been performed by making use of various visual methods (Kline *et al.* 1967; Corino & Brodkey 1969; Kim, Kline & Reynolds 1971; Grass 1971; Nychas, Hershey & Brodkey 1973; Offen & Kline 1975; Nakagawa & Nezu 1977*b*; Praturi & Brodkey 1978; and others) and conditional point measurements by hot-wire or hot-film anemometers (Gupta, Laufer & Kaplan 1971; Lu & Willmarth 1973; Brodkey, Wallace & Eckelmann 1974; Blackwelder & Kaplan 1976; Sabot & Comte-Bellot 1976; Wallace, Brodkey & Eckelmann 1977; Nakagawa & Nezu 1977*a*, 1978; and others). As the result of this research, the physics of solid-wall turbulence has now been fairly established, at least in a qualitative sense. For example, Hinze (1975), Laufer (1975) and Willmarth (1975) have written excellent reviews which describe the recent status of research on solid-wall turbulence, especially on the bursting phenomenon of tubulent boundary layers. Also, they have pointed out the necessity of research on the structure of the instantaneous Reynolds stress in order to make clear the bursting phenomenon near the wall. The authors (Nakagawa & Nezu 1977*a*) have investigated in detail the contributions to the Reynolds stress from bursting events in open-channel flows by conditionally analysing the instantaneous Reynolds-stress fluctuations obtained from the hot-film anemometers. In 1978 they proposed a new evaluation method for the bursting period, on the basis of the phenomenological consideration that the number of the occurrences

0022-1120/81/4576-3130 $02.00

of interaction-like motions should be removed from those of the ejection and sweep events in the sorted Reynolds-stress fluctuating signals. Then, they examined the periodic characteristics of the bursting phenomenon in the Eulerian observation, i.e. the passing-period, by systematically varying the Reynolds and Froude numbers as well as the wall roughness.

Several theoretical models by which the mechanism of wall turbulence and the bursting process can be explained even quantitatively have been proposed, on the basis of much experimental knowledge of the bursting phenomenon. These models may be roughly classified into two groups. One is a renewal model which was originally proposed by Einstein & Li (1956), and the other is a waveguide model which was originally proposed by Landahl (1967). Black (1968) developed a renewal model in which the formation and breakdown of the horseshoe vortex were considered in a repetitive way. He could successfully explain several turbulence characteristics even quantitatively, although the governing equation was one-dimensional and linear, similar to the Einstein–Li model. Recently, the authors (Nakagawa & Nezu 1978) also proposed a modified renewal model which was inherently quasi-two-dimensional and quasi-linear in regard to the streamwise and normal velocities u and v, on the basis of the Einstein–Li model and also the knowledge of the bursting-period characteristics. They could satisfactorily explain fairly well, even quantitatively, a sequence of the bursting process near the wall, as well as the distributions of mean velocity, turbulence intensities, Reynolds stress, etc.

On the other hand, a waveguide model was developed by Bark (1975) and Landahl (1977). They considered the wave-type motions with Fourier components and derived a linear non-homogeneous Orr–Sommerfeld equation in which the nonlinear terms of Reynolds stress were regarded as a known forcing function. Then, by assuming that these nonlinear forcing terms, i.e. the instantaneous Reynolds stresses, were a random distribution of delta functions in the streamwise and spanwise directions x, z and the time t with a variation with the normal direction y inferred from the experimental data, they could theoretically obtain the spectral distributions of fluctuating velocities, which were in good agreement with the experimental values. Although the waveguide model seems to be more sophisticated than the renewal model, the former cannot probably explain the bursting mechanism better than the latter, because the bursting process itself is considered as a known driving force of the turbulent flow.

It should be noticed that both the renewal and waveguide models are applicable only very near the wall, i.e. $y^+ \leqslant 50$, since their models are inherently approximated by linear differential equations. However, a closer interrelation between the inner and outer layers, i.e. between the bursting and bulge motions in boundary layer, has been suggested through the visual observations or the hot-wire measurements by Laufer & Narayanan (1971), Blackwelder & Kovasznay (1972), Offen & Kline (1975), Falco (1977), Brown & Thomas (1977) and Praturi & Brodkey (1978). A closer interrelation between the wall and free-surface regions, i.e. the bursting and boil phenomena in an open channel, has been also suggested by Grass (1971), Jackson (1976) and Nakagawa & Nezu (1978).

Figure 1 shows an illustration of the coherent structures in an open-channel flow, on the basis of previous visual observations. The most notable characteristics are that (1) the bursting period T_B and the streamwise spacing λ_x of the bursting motions in an open-channel flow are controlled by the outer parameters such as the flow depth h and

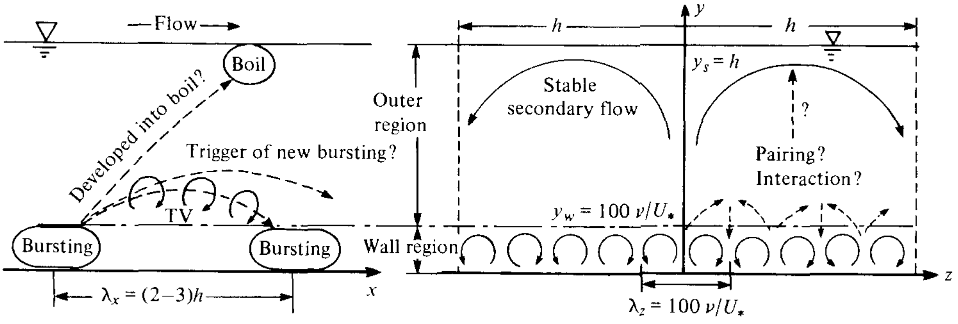

FIGURE 1. Illustration of the coherent structures in an open-channel flow.

the maximum velocity $U_{\max}$, while its spanwise spacing λ_z is controlled by the inner parameters of ν/U_* (Nakagawa & Nezu 1978), and (2) the boil or stable secondary flow appears at a nearly fixed position on the free surface and it is controlled by the outer parameters (Kinoshita 1967; Jackson 1976). From these visual results, the following essential and important questions are produced.

(1) Does a bursting motion grow to be a transverse vortex (TV) in the outer region, and in turn does its vortex generate a new bursting motion at the downstream in the wall region?

(2) Does a strong bursting motion develop up to the free surface and then become a boil?

Therefore, an investigation of the space–time structure of the bursting phenomenon, which occurs originally near the buffer layer and then shows a coherent or organized flow structure during its convection process, will be contributive not only to the confirmation of these suggestions, but also the refinement of physical description of the bursting phenomenon.

In the light of the above, the present study is to investigate the structure of space–time correlations of bursting events, such as ejections and sweeps in an open-channel flow by the conditional sampling of the instantaneous Reynolds-stress signals measured simultaneously at two different points. One probe is fixed near the edge of the buffer layer and used as a detecting probe of the bursting motions, and the other probe is moved in both the streamwise and vertical directions. The temporal and spatial scales of the ejection and sweep motions, their convective characteristics and the spanwise spatial properties of the high-speed and low-speed streaks in the bursting motions will be experimentally investigated. A qualitative model will be then proposed which attempts to explain the space–time structure of the bursting phenomenon in an open-channel flow.

2. Analytic technique

2.1. *Conventional space–time correlations*

We consider a fully developed, two-dimensional and normal open-channel flow field, as shown in figure 1. The x co-ordinate is aligned with the mainstream velocity or the free-surface velocity $U_{\max}$. The co-ordinate y is perpendicular to the wall, and z is in the spanwise direction. The velocity fluctuations in the x, y and z directions are u, v and w, and their r.m.s. values, i.e. the turbulence intensities, are u', v' and w', respectively.

Since the veloocity field is homogeneous in the streamwise (x axis) and spanwise (z axis) directions and is also steady in time, the conventional space–time correlations of the velocity components $u_i(x_0, y_0, z_0, t_0)$ and $u_j(x_1, y_1, z_1, t_1)$ are defined by

$$\begin{aligned} C_{u_i u_j}(\Delta x, y_0, y_1, \Delta z, \tau) &= \frac{\overline{u_i(x_0, y_0, z_0, t_0) \, . \, u_j(x_1, y_1, z_1, t_1)}}{u_i'(x_0, y_0, z_0)\, u_j'(x_1, y_1, z_1)} \\ &\equiv \overline{\hat{u}_i(x_0, y_0, z_0, t_0)\, \hat{u}_j(x_0+\Delta x, y_1, z_0+\Delta z, t_0+\tau)}, \end{aligned} \tag{1}$$

where suffixes i and j are 1, 2 or 3, i.e. $u_1 = u$, $u_2 = v$ and $u_3 = w$. $\hat{u}_i$ is the velocity fluctuation normalized by its turbulence intensity u_i', that is, $\hat{u}_i \equiv u_i/u_i'$. $\Delta x \equiv (x_1 - x_0)$, $(y_1 - y_0)$ and $\Delta z \equiv (z_1 - z_0)$ are the spatial separations, and $\tau \equiv (t_1 - t_0)$ is the time lag. The signal $u_i(x_0, y_0, z_0, t_0)$ from the fixed probe was recorded and shifted in time. It was then correlated with the signal $u_j(x_1, y_1, z_1, t_1)$ from the movable probe which was located upstream or downstream. Of course, by denoting that $i = 1, j = 2, y_0 = y_1 = y$ and $\Delta x = \Delta z = \tau = 0$, we can obtain the correlation coefficient of the Reynolds stress $-\overline{uv}$, as follows:

$$R(y) \equiv \frac{-\overline{uv}}{u'v'} = -C_{uv}(0, y, y, 0, 0) = -\overline{\hat{u}(y,t)\,\hat{v}(y,t)}. \tag{2}$$

2.2. *A new conditional analysis of space–time correlations*

Although the bursting phenomenon occurs fairly random at one place or time, a sequence of its bursting events has a quasi-ordered process. It seems, therefore, that its significant information cannot be obtained by the conventional 'long-time' averaging technique such as (1), as has been pointed out by many researchers. Hence, a conditional sampling method which detects the significant information from the fluctuating velocity signals has been explored by Kovasznay, Kibens & Blackwelder (1970). In general, the conditional average of an arbitrary signal $q(x_1, y_1, z_1, t+\tau)$ can be defined as follows:

$$\langle q \rangle (x_1, y_1, z_1, \tau) = \frac{\int_T q(x_1, y_1, z_1, t+\tau)\, I(x_0, y_0, z_0, t)\, dt}{\int_T I(x_0, y_0, z_0, t)\, dt}, \tag{3}$$

where, $\int_T \ldots dt$ means $\lim_{T\to\infty} T^{-1} \int_0^T \ldots\, dt$. The function $I(x_0, y_0, z_0, t)$ detects the turbulence phenomenon in question which occurs at the point of (x_0, y_0, z_0, t). For example, the detecting function $I(x_0, y_0, z_0, t)$ of the bulges phenomenon in the boundary layer can be definitely given by the intermittency function (e.g. Blackwelder & Kovasznay 1972), as follows:

$$I(x_0, y_0, z_0, t) = \left\{ \begin{matrix} 1 & \text{for turbulent flow,} \\ 0 & \text{for non-turbulent flow.} \end{matrix} \right\} \tag{4}$$

However, the detecting function I of the bursting phenomenon near the wall is not yet sufficiently established at present, although several detecting functions have been proposed by Lu & Willmarth (1973), Brodkey *et al.* (1974), Blackwelder & Kaplan (1976), Wallace *et al.* (1977), Nakagawa & Nezu (1978) and others. As already pointed out in our 1978 paper, the instantaneous Reynolds-stress signals $u(t)\,v(t)$ can be reasonably used as discriminating information, since they are directly related to the bursting phenomenon or the mechanism of turbulence production. Then, the sorting functions of ejection, $I_e(t)$, sweep, $I_s(t)$, outward interaction, $I_0(t)$, and inward interaction, $I_i(t)$, are defined, respectively, as follows:

$$I_e(t) \equiv I_2(t) = \begin{cases} 1 & \text{for} \quad u(t) < 0 \quad \text{and} \quad v(t) > 0, \\ 0 & \text{otherwise;} \end{cases} \tag{5}$$

$$I_s(t) \equiv I_4(t) = \begin{cases} 1 & \text{for} \quad u(t) > 0 \quad \text{and} \quad v(t) < 0, \\ 0 & \text{otherwise;} \end{cases} \tag{6}$$

$$I_0(t) \equiv I_1(t) = \begin{cases} 1 & \text{for} \quad u(t) > 0 \quad \text{and} \quad v(t) > 0, \\ 0 & \text{otherwise;} \end{cases} \tag{7}$$

$$I_i(t) \equiv I_3(t) = \begin{cases} 1 & \text{for} \quad u(t) < 0 \quad \text{and} \quad v(t) < 0, \\ 0 & \text{otherwise.} \end{cases} \tag{8}$$

Here, the ejection (another term of 'burst' or lifted wall streak, *cf.* Kline *et al.* 1967) and sweep events are mainly considered, because these events contribute mostly to the Reynolds stress or the turbulence production.

Unfortunately, $I_e(t)$ or $I_s(t)$ should not be regarded directly as a detecting function $I(t)$ for the bursting motions, because the ejection and sweep events in the sorted Reynolds-stress signals still contain the interaction-like motions, as has been pointed out in our (1978) paper. So, Lu & Willmarth (1973), Sabot & Comte-Bellot (1976) and Nakagawa & Nezu (1977*a*, 1978, 1979) introduced a threshold level H in the Reynolds-stress signals, and assumed that the bursting motions occur only when $|u(t)\,v(t)| \geqslant H$. However, the determination of the threshold level H is more or less arbitrary. Therefore, we adopt a new detecting function weighted by the instantaneous Reynolds-stress signal itself, i.e. $I(t) \equiv u(t)\,v(t)\,I_e(t)$, etc. Then, the conditional average of the space–time correlations of ejection and sweep motions can be definitely given by, respectively,

$$\langle q \rangle_e(x_1, y_1, z_1, \tau) = \frac{\int_T q(x_1, y_1, z_1, t+\tau) . \{u(t)\,v(t)\,I_e(t)\}_0\,dt}{\int_T \{u(t)\,v(t)\,I_e(t)\}_0\,dt}, \tag{9}$$

$$\langle q \rangle_s(x_1, y_1, z_1, \tau) = \frac{\int_T q(x_1, y_1, z_1, t+\tau)\,\{u(t)\,v(t)\,I_s(t)\}_0\,dt}{\int_T \{u(t)\,v(t)\,I_s(t)\}_0\,dt}, \tag{10}$$

where, the suffix $\{\ \}_0$ denotes the position of the detecting probe. (9) or (10) means that the stronger the instantaneous Reynolds stress is, the larger contribution is given in the average structure of the bursting phenomenon.

Such a weighted detecting function seems to be more useful and reasonable than a detecting function with a threshold level H. This is because a more objective evaluation can be carried out without arbitrary parameters. Also, the random values such as the background turbulence are apt to cancel each other because of the larger numbers of data averaged than in the case of $|u(t)\,v(t)| \geqslant H$. Recently, Nezu & Nakagawa (1981) have made a detailed comparison between the threshold method of H, VITA-method of Blackwelder & Kaplan (1976), and pattern recognition method of Wallace, Brodkey & Eckelmann (1977) and the present weighted-average method. The obvious validity of (9) and (10) will be shown through the following experimental considerations.

3. Experimental equipment and procedures

Two groups of experiments on a two-dimensional, fully developed and normal turbulent flow in a smooth open channel, whose hydraulic conditions are described in table 1, were conducted in a tilting flume 15 m long, 50 cm wide and 30 cm deep at the Hydraulics Laboratory of Civil Engineering in Kyoto University. This experimental set-up was the same as that previously used by Nakagawa & Nezu (1977*a*, 1978, 1979). A settling chamber and screens to prevent the occurrence of large-scale disturbances and the distortion of main surface flow were set up at the entrance of the channel, and consequently a fully developed turbulent flow was obtained at the test section 9·5 m downstream from the entrance.

In one group of the experiments (case QV), the correlations between (u_0, v_0) and (u_1, v_1) at a couple of points in the x, y centre-plane of the channel (i.e. $z_0 = z_1 = 0$, see figure 1) were measured by using two sets of dual-sensor hot-film anemometers (DISA 55M-SYSTEM), i.e. an X-type probe (DISA 55R64) and a V-type probe (DISA 55A89). The flow depth h was 8 cm and the mean velocity U_m was 15 cm s^{-1}. As for results, the Reynolds number was $R_e \equiv U_m h/\nu = 1{\cdot}2 \times 10^4$ or $R_* \equiv U_* h/\nu = 774$ (where U_* is the friction velocity). The Froude number was $Fr \equiv U_m/\sqrt{(gh)} = 0{\cdot}17$. These hydraulic conditions were nearly the same as those in our previous studies (1977*a*, 1978).

A reasonable configuration of these hot-film probes was prepared in order to avoid any interference from the wake of the upstream probe. As shown in figure 2, the X-type fibre-film probe with two pairs of needles of 9·1 mm length was adopted as the upstream probe. The V-type wedge-film probe with 100 mm straight length in the streamwise direction was used as the downstream probe. The rod of the upstream probe with 2·3 mm diameter and 65 mm length was laid in the x, z plane and perpendicular to the x axis (see figure 2*c*). Two probes were spaced about 2 mm in the spanwise direction when Δx was comparatively small so as to move the probe easily. Thus, the small wakes behind the needles of the upstream probe will hardly influence the downstream probe. However, it was suggested that this separation distance of Δz was so large that $C_{uu}(\Delta x, y_0, y_1, \Delta z, \tau)$ cannot be regarded even approximately as $C_{uu}(\Delta x, y_0, y_1, 0, \tau)$ when Δx was small.

The detecting probe was fixed at $y_0 = 0{\cdot}4$ cm ($y_0/h = 0{\cdot}05$, $y_0^+ \equiv y_0 U_*/\nu = 38$), since the bursting phenomenon, such as the ejections and sweeps, occurs most violently below or near this position (e.g. Corino & Brodkey 1969). The movable probe was set at the different 222 points in number in the x, y plane. That is, $y_1 = 0{\cdot}4$, 0·7, 1·3, 2·4, 4·0 and 6·0 cm, which were the representative points in the wall region ($y^+ \leqslant 100$), the equilibrium region ($100 \leqslant y^+$ and $y/h \leqslant 0{\cdot}6$) and the free-surface region ($y/h \geqslant 0{\cdot}6$) (see Nezu 1977*a*). From the fact that the streamwise spacing scale λ_x of the bursting phenomenon was the order of $4h$ (see Hinze 1975, p. 682; Nakagawa & Nezu 1978), $|\Delta x|$ was varied up to $4h$ so as to be smaller in the neighbourhood of the fixed probe. A more detailed description of these experimental techniques is given in Nakagawa, Nezu & Matsumoto (1980).

Next, we should examine the spanwise spatial structure in the y, z plane, i.e. the structure of the high-speed and low-speed streaks, as shown in figure 1. For this purpose, we have conducted nearly the same experiments of $R_e = 4230$ and $1{\cdot}1 \times 10^4$ (case R, see table 1) as those of case QV, by making use of the same hot-film probes. In this case,

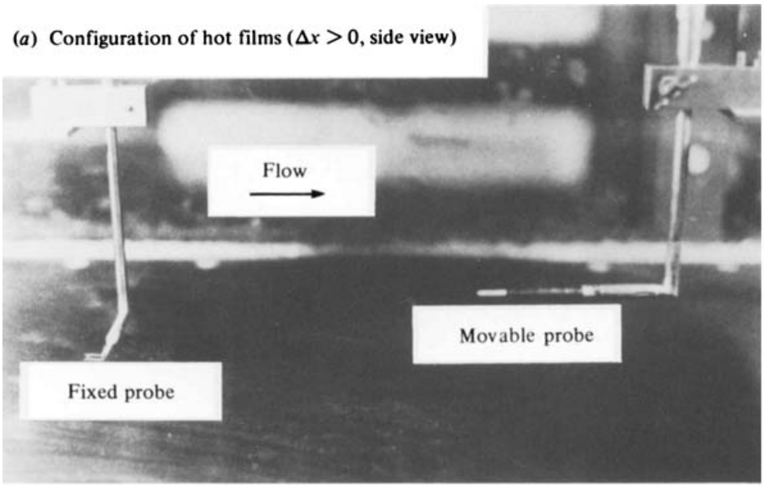
(*a*) Configuration of hot films ($\Delta x > 0$, side view)

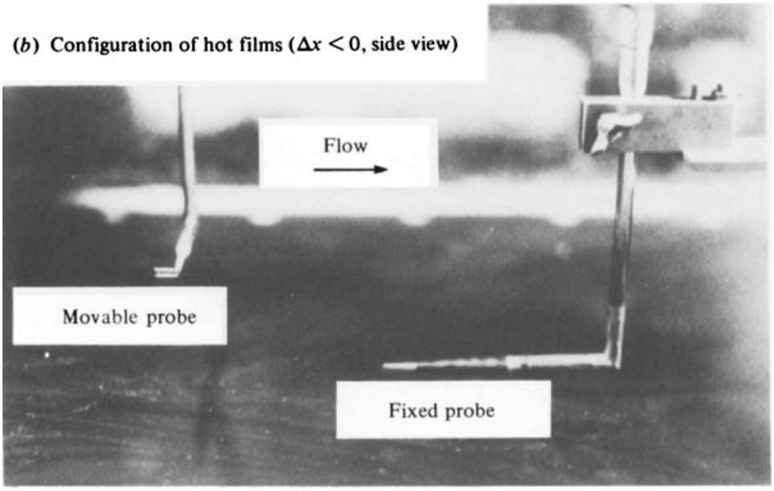
(*b*) Configuration of hot films ($\Delta x < 0$, side view)

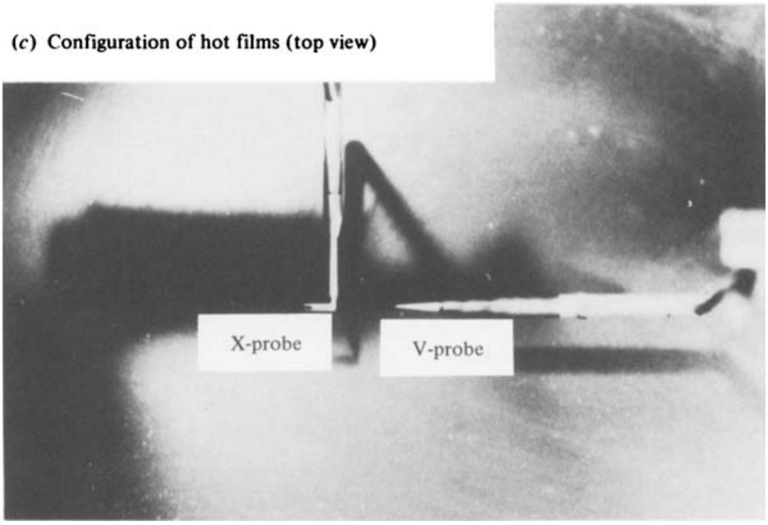
(*c*) Configuration of hot films (top view)

FIGURE 2. Configuration of two hot-film probes. The upstream probe is an X-type fibre hot-film, while the downstream probe is a V-type wedge hot-film.

Series of experiments	Case QV (x, y plane)	Case R-1 (y, z plane)	Case R-2 (y, z plane)
Flow depth h (cm)	8·1	7·7	7·9
Discharge Q ($\mathrm{l\,s^{-1}}$)	6·0	5·5	2·2
Free-surface velocity $U_{\max}$ ($\mathrm{cm\,s^{-1}}$)	21·2	20·4	8·4
Mean velocity U_m ($\mathrm{cm\,s^{-1}}$)	14·9	14·1	5·5
Friction velocity U_* ($\mathrm{cm\,s^{-1}}$)	0·95	0·94	0·42
Reynolds number $R_e \equiv U_m h/\nu$	$1{\cdot}2\times10^4$	$1{\cdot}1\times10^4$	$0{\cdot}42\times10^4$
$R_* \equiv U_* h/\nu$	774	696	318
Froude number $F_r \equiv U_m/(gh)^{\frac{1}{2}}$	0·17	0·16	0·063
Water temperature T_w (°C)	20·7	18·7	19·6

TABLE 1. Hydraulic parameters for the experiments.

the vertical positions of the fixed and movable probes were set equally to each other, in which $y \equiv y_0 \equiv y_1 = 0{\cdot}4$, $0{\cdot}7$, $1{\cdot}3$, $2{\cdot}4$, $4{\cdot}0$ and $6{\cdot}0$ cm, again. Also, the position z_0 of the fixed probe was set at the centre of the channel, i.e. $z_0 \equiv 0$, $z_1 \equiv \Delta z \equiv z$, while the movable probe was set at the different 87 points in number in the y, z plane, i.e. $x_0 \equiv x_1 = 0$.

The output signals of the anemometers were recorded in analog form by using an FM tape recorder for about two minutes at each measured point. The effects of impurities or bubbles in the water on the hot-films were almost negligible in this duration, and thus a most stable operation of the anemometers was obtained. The output signals were then reproduced for converting into digital form, with the sample size $N = 10000$ and the sampling frequency $f = 100$ Hz, that is, the average-evaluation time $T = N/f = 100$ seconds. This sampling frequency f was chosen so that the spectral analysis could become possible at least to the extent of the inertial subrange (Nezu 1977*a*; Nakagawa & Nezu 1978).

For all measurements, the temperature difference between the water (T_w) and the hot-film sensor (T_s) was set about 20 °C. The maximum frequency response $f_{\max}$ of the hot-films is 30 kHz in the technical data of DISA, and it was confirmed by the spectral analysis (Nezu 1977*a*) that $f_{\max} > 1000$ Hz in our hydraulic conditions, which is sufficiently high for the present study. The hot-film anemometers were calibrated by towing the probe over a fixed length (about 2 m) in still water, by making use of a movable carriage driven by a variable motor before and after each series of measurements.

Consequently, the output voltage signals could be easily converted into the velocity signals through these calibration curves. Then, some statistical analyses described previously were carried out by a large digital computer, the FACOM M-190, at the Data Processing Center, Kyoto University. Most of the results were then plotted by an on-line X–Y plotter.

4. Experimental results and discussion

4.1. *Examination of some basic quantities of turbulence*

Figure 3 shows the mean velocity distributions $U^+ = U/U_*$ measured by the V-type probe in the centre-line ($z = 0$) of the channel. The solid line is the well-known log-law distribution, which is given by the van Driest type for $y^+ \leqslant 30$, where von Kármán's constant $\kappa = 0{\cdot}4$ and van Driest's constant $A = 27$ are used (e.g. Rotta

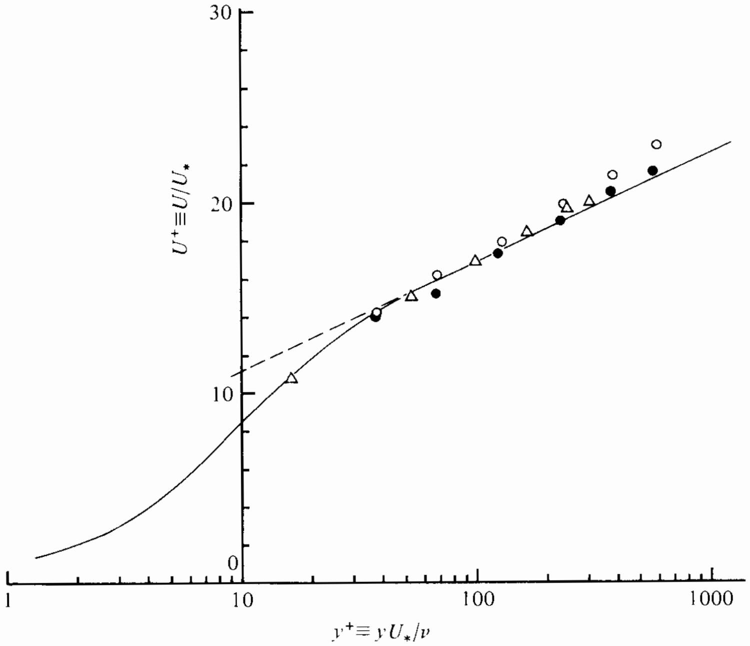

FIGURE 3. Mean velocity distribution, $U^+ \equiv U/U_*$ *vs.* y^+ (the law of the wall). ○, Case QV; ●, Case R-1; △, Case R-2; ——, van Driest's curve; – – –, $U^+ = 5{\cdot}75 \log y^+ + 5{\cdot}5$.

1972). The experimental values in the wall region ($y^+ \leqslant 100$) agree very well with the logarithmic profile, although they show a little deviation from this profile in the outer region. Hence, the friction velocity U_* could be evaluated from this logarithmic distribution.

In the present study of cases R-1 and R-2, the spanwise measurements of the mean velocity did not show any significant features to confirm an existence of the stable cellular secondary flow (see figure 1). Our recent study (Nezu, Nakagawa & Tominaga 1980; Nakagawa & Nezu 1980) suggests strongly that a stable cellular secondary flow may be very weak in a laboratory straight-line smooth flume with low Reynolds number. In other words, a loose and rough bed is necessary to examine clearly an existence of this secondary flow in an open-channel flow, as has been suggested by Müller (1977).

Next, the crude values of the Reynolds stress $-\overline{uv}/U_*^2$ measured by the dual hot-films are shown in figure 4. These experimental values agree fairly well with the theoretical curve which is described by

$$\frac{-\overline{uv}}{U_*^2} = (1-y/h) - \frac{2(1-y^+/R_*)}{1+[1+4l^{+2}(1-y^+/R_*)]^{\frac{1}{2}}}, \qquad (11)$$

where, l^+ is the dimensionless mixing-length, which is given again by the van Driest type (see Nezu 1977*a* or Nakagawa & Nezu 1979). It is more desirable, however, to correct the calibration coefficients of each hot-film sensor which were separately determined by the carriage-calibration method, so that the output data of $-\overline{uv}$ obtained from the cross-operation of each sensor signal may coincide perfectly with the theoretical values of (11), on the invariant condition of u' and v'. This is because the

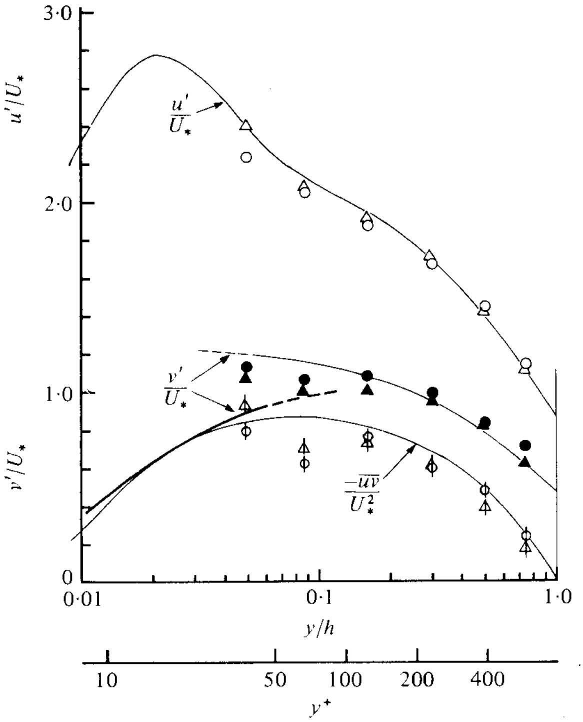

FIGURE 4. Distributions of turbulence intensities u'/U_*, v'/U_* and Reynolds stress $-\overline{uv}/U_*^2$. The values measured by V-type hot-films: ○, u'/U_*; ●, v'/U_*; ϕ, $-\overline{uv}/U_*^2$. The values measured by X-type hot-films: △, u'/U_*; ▲, v'/U_*; ⍋, $-\overline{uv}/U_*^2$. ——, theoretical curves of equations (11), (12) and (13).

output signals of $u(t)\,v(t)$ are essential quantities for investigating the bursting phenomenon, as mentioned previously. In the present experiment, this correction of the calibration coefficients was within only 5 %.

Figure 4 shows also the experimental values of the turbulence intensities u'/U_* and v'/U_*, which are ensemble-averaged among the data obtained at all streamwise positions x_1 for each height y_1. The authors have derived the theoretical curves of the turbulence intensities in the Π-eddy model (1974), the combined model (Nezu 1977*a*) and the renewal model (1978), as follows:

$$\frac{u'}{U_*} = (1-\exp(-y^+/A))\,D_1\exp(-y^+/R_*)+\exp(-y^+/A)\,By^+, \tag{12}$$

$$\frac{v'}{U_*} = D_2\exp(-y^+/R_*) \quad \text{for} \quad y^+ > 50, \tag{13a}$$

$$\frac{v'}{U_*} = \frac{\gamma^{\frac{1}{4}}}{2\alpha U_0^+(1+\beta)^{\frac{1}{2}}}\left[\int_{-\infty}^{\infty}\frac{G(S)}{10^{\sigma_0 S}}\,dS\int_0^1\frac{(1-\exp(-\Theta^2))^2}{\tau}\,d\tau + \frac{1}{\beta}\left\{\int_{-\infty}^{\infty}\frac{G(S)}{10^{\sigma_0 S/2}}\,dS\int_0^1\frac{(1-\exp(-\Theta^2))}{\tau^{\frac{1}{2}}}\,d\tau\right\}^2\right]^{\frac{1}{2}} \quad \text{for} \quad y^+ \leqslant 50. \tag{13b}$$

In the above, $A = 10$, $B = 0{\cdot}3$, $D_1 = 2{\cdot}3$ and $D_2 = 1{\cdot}27$, and

$$\Theta \equiv \frac{\pi^{\frac{1}{2}}}{4}\gamma^{\frac{1}{4}}y^+/(U_0^+ . 10^{\sigma_0 S/2}\tau^{\frac{1}{2}}),$$

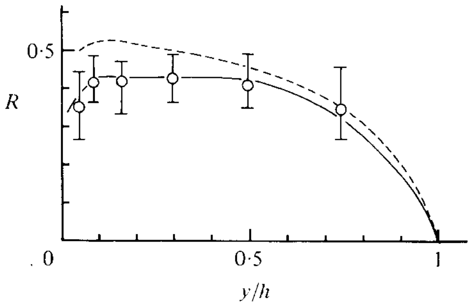

FIGURE 5. Correlation coefficient of the Reynolds stress, $R = -\overline{uv}/U_*^2$. The present data ($Re = 1{\cdot}2\times10^4$, smooth open-channel): ○, mean value; T, maximum value; ⊥, minimum value. Laufer (1954): – – –, $Re = 2{\cdot}2\times10^4$ (smooth pipe). Bremhorst & Walker (1973): —— $Re = (2{\cdot}3\text{–}9{\cdot}0)\times10^4$ (smooth pipe).

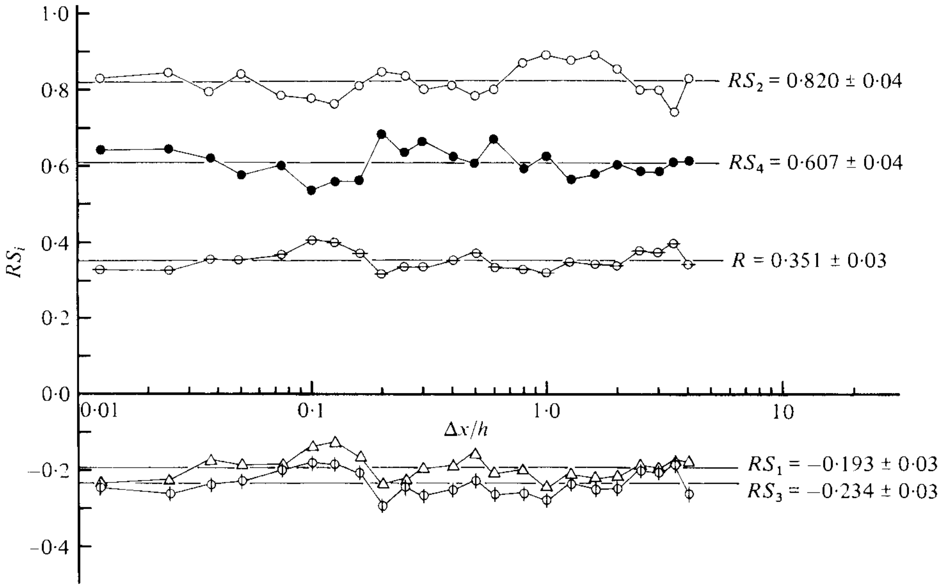

FIGURE 6. Contribution rates RS_i (i = 1, 2, 3, 4) of each bursting event to the Reynolds stress obtained at $y^+ = 38$. △, RS_1 (outward interaction); ○, RS_2 (ejection); ⦶, RS_3 (inward interaction); ●, RS_4 (sweep); ⊖, R (correlation coefficient of the Reynolds stress, see figure 5).

$$G(S) \equiv (2\pi)^{-\frac{1}{2}}\exp(-S^2/2),$$
$$\sigma_0 \equiv (\log_{10}e)(\ln(1+\psi^2))^{\frac{1}{2}}, \quad \gamma \equiv (1+\psi^2)^{-\frac{1}{2}},$$

$G(s)$ is an averaging weighted function in which the probability of the occurrence of bursting process is assumed to be expressed by a log-normal distribution. Then, ψ is the coefficient of variation of the bursting period, i.e. $\psi \equiv \sigma_B/T_B$, and it is nearly equal to 0·5–1·5. U_0^+ is the mean velocity of the main flow at the edge of the wall region, that is, $U_0^+ = 15$. Also, $\alpha \equiv U_c/U_0 = 0{\cdot}7$ (where U_c is the convection velocity of the coherent vortex motions), and $\beta \equiv T_2/T_1 = 0{\cdot}01$ (where T_1 and T_2 are the built-up and the breakdown durations of the coherent vortex motions, respectively). A more detailed description of this renewal model is given in Nakagawa & Nezu (1978).

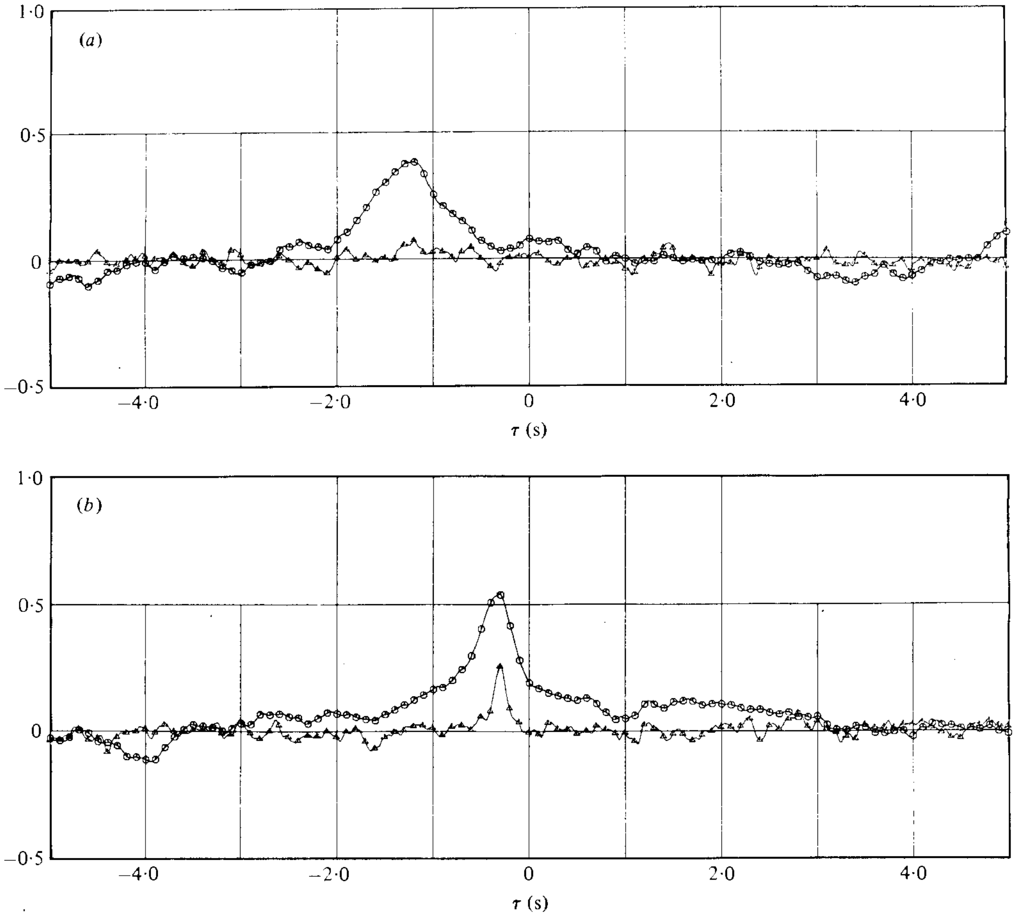

FIGURE 7 (a, b). For the caption see the next page.

The experimental values of u'/U_* and v'/U_* measured by both the X-type and V-type probes are in good agreement with (12) and (13), as well as the data measured in detail by Laufer (1954) and Nezu (1977*b*).

Figure 5 shows the correlation coefficient $R(y)$ of the Reynolds stress which is given by (2). The scatter among these data at the different positions x_1 is shown by the maximum, mean and minimum values. Their mean values agree well with the experimental values given by many researchers (e.g. Laufer 1954; Bremhorst & Walker 1973; Nezu 1977*a*). Also, the scatter of the present data is almost within that of the previous data.

Furthermore, in order to examine the interference of the wake of the upstream probe, the contribution rates RS_j of each bursting event to the Reynolds stress are shown in figure 6, as a function of $\Delta x/h$ for $y_0/h = y_1/h = 0{\cdot}05$. They are the essential characteristic values, on analysing the bursting phenomenon, and are defined as follows:

$$RS_j = \overline{u(t)\,v(t)\,I_j(t)}/\overline{u(t)\,v(t)} \quad (j = 1, 2, 3, 4), \tag{14}$$

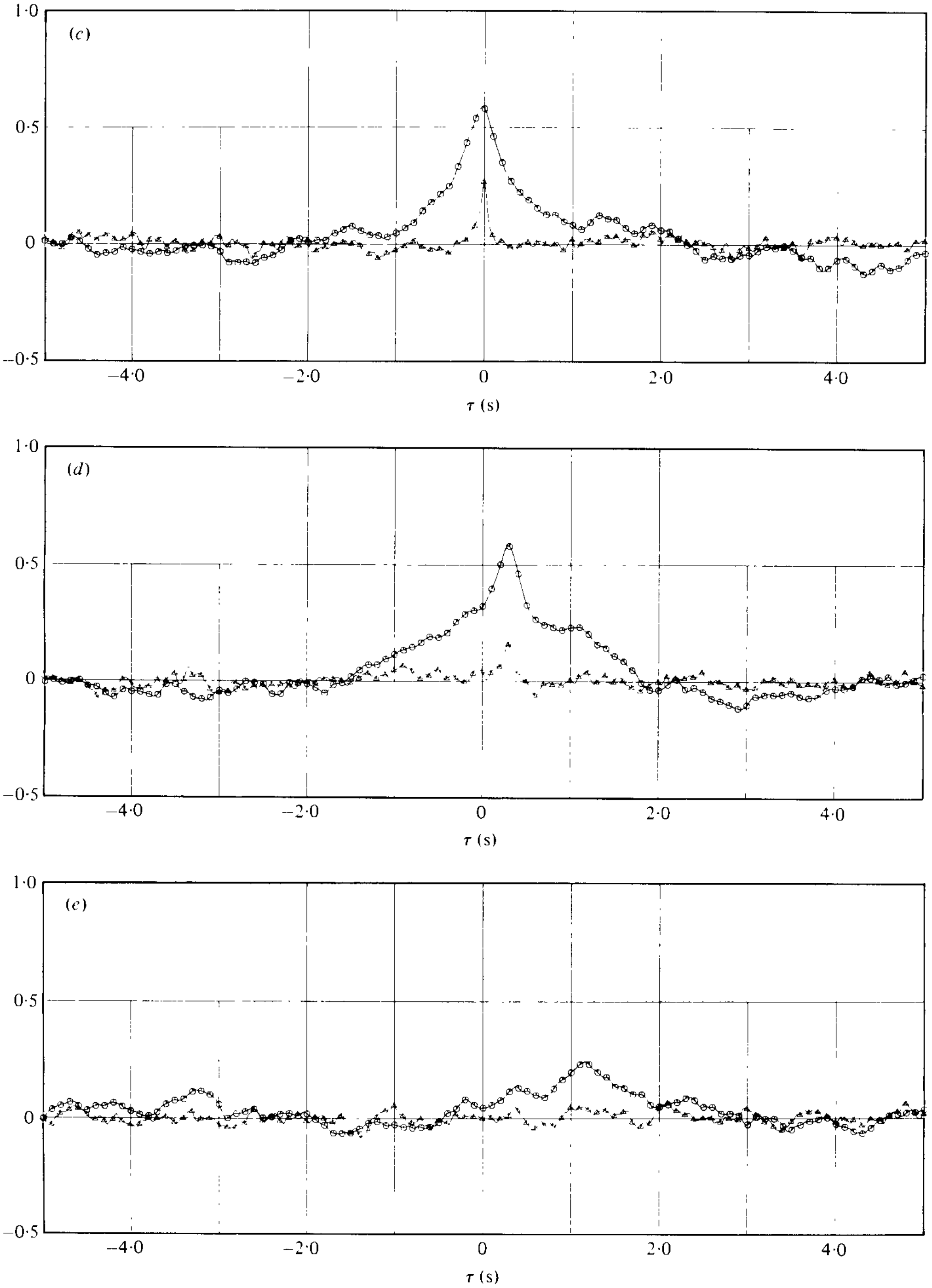

FIGURE 7. Conventional long-time averaging space–time correlations of u and v: ⊖, $C_{uu}(\Delta x, \tau)$; ▲, $C_{vv}(\Delta x, \tau)$; $y_{\text{fix}} = 0{\cdot}4$ cm, $y_{\text{mov}} = 0{\cdot}7$ cm. (*a*) $\Delta x = -16{\cdot}0$ cm, (*b*) $\Delta x = -4{\cdot}0$ cm, (*c*) $\Delta x = 0{\cdot}0$ cm, (*d*) $\Delta x = 4{\cdot}0$ cm, (*e*) $\Delta x = 16{\cdot}0$ cm.

where $j = 1$ (outward interaction), $j = 2$ (ejection), $j = 3$ (inward interaction) and $j = 4$ (sweep). So, $I_j(t)$ is given by (5)–(8). The mean value and its standard deviation of RS_j are also described in figure 6, respectively. Variation of the measured data of RS_j does not show any systematic trend against $\Delta x/h$ even when Δx is small. Also, the present values of RS_j agree well with previous experimental and theoretical values given by Nakagawa & Nezu (1977*a*).

From the above examinations, it may be concluded that the present turbulence measurements by both the X-type and V-type probes are fairly accurate in at least one-point measurement, and that the interference of the wake of the upstream probe is almost negligible.

4.2. *Conventional space–time correlations*

Figure 7 shows some typical examples of the conventional space–time correlations $C_{uu}(\Delta x, y_{\mathrm{fix}}, y_{\mathrm{mov}}, \tau)$ and $C_{vv}(\Delta x, y_{\mathrm{fix}}, y_{\mathrm{mov}}, \tau)$ which were plotted by the X–Y plotter. In figure 8, $C_{uu}(\Delta x, \tau)$ at $y_0/h = y_1/h = 0{\cdot}05$ is described in a three-dimensional picture, where $C_{uu} > 0$ and $C_{uu} < 0$ are separately described by the solid and broken lines, respectively. From these figures, the spatial scales and the convection process of the u or v velocity component can be obtained in terms of long-time averaging structure, and they are also compared with many previous results given by Favre (1965), Blackwelder & Kovasznay (1972), etc.

Firstly, the correlation of the v component decays faster in both space and time than does that of the u component. Figure 9 shows the space correlations $C_{uu}(\Delta x, \tau = 0)$ and $C_{vv}(\Delta x, \tau = 0)$ at $y_0/h = y_1/h = 0{\cdot}05$. The mean eddy scale L_u and L_v of u and v are defined, respectively, as follows:

$$L_u = \int_0^{x_{0u}} C_{uu}(\Delta x)\, d(\Delta x), \quad L_v = \int_0^{x_{0v}} C_{vv}(\Delta x)\, d(\Delta x), \qquad (15), (16)$$

where x_{0u} and x_{0v} are the separation distances up to the zero-cross of $C_{uu}(\Delta x)$ and $C_{vv}(\Delta x)$, respectively. In this case, $L_u/h = 0{\cdot}31$ and $L_v/h = 0{\cdot}075$ are obtained. This value of L_u/h is in good agreement with the previous values, and of course, it is much larger than L_v/h. If C_{uu} and C_{vv} can be approximated by an exponential function, then $C_{uu}(\Delta x) = \exp(-\Delta x/L_u)$ and $C_{vv}(\Delta x) = \exp(-\Delta x/L_v)$, which are shown by the broken lines in figure 9. Although the measured data can be roughly described by the exponential function, a large difference between the two appears when Δx is small, i.e. $\Delta x \leqslant 1$ cm.

Since the perturbations or the turbulent eddies are convected with a velocity U_c, the peak of C_{uu} or C_{vv} appears at a time lag for any separation Δx, which is referred to the optimum delay τ_{opt}, as shown in figure 8. Figure 10 shows $C_{uu}(\Delta x, \tau_{\mathrm{opt}})$ and $C_{vv}(\Delta x, \tau_{\mathrm{opt}})$ in this convected Eulerian frame. Indeed, the correlation of the v component decays rapidly and disappears. On the other hand, the correlation of u decays much more slowly, and does not disappear within the present measurement interval of $\Delta x/h \simeq 4$.

Blackwelder & Kovasznay (1972) pointed out that $C_{uu}(\Delta x, \tau_{\mathrm{opt}})$ and $C_{vv}(\Delta x, \tau_{\mathrm{opt}})$ in the main region of the boundary layer could be well described by the sum of two exponential functions with decay rates differing by approximately one order of magnitude. The rapidly decaying curve is for the small eddies, while the slowly decaying curve is for the large eddies. However, the present results indicate only the slowly decaying exponential curve, as shown in figure 10. The $1/e$ folding separation for this large eddy structure is then $\Delta x = 2{\cdot}6h$ and h for C_{uu} and C_{vv}, respectively. These values

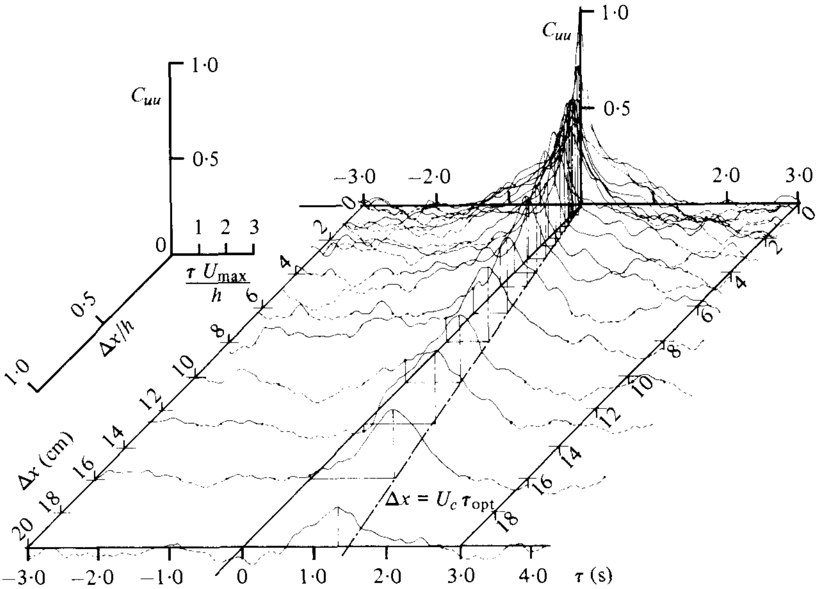

FIGURE 8. Longitudinal space–time correlation of $C_{uu}(\Delta x, \tau)$ obtained at $y^+ = 38$; $y/h = 0{\cdot}05$. ——, $C_{uu} > 0$; – – –, $C_{uu} < 0$; —·—, optimum delay τ_{opt}.

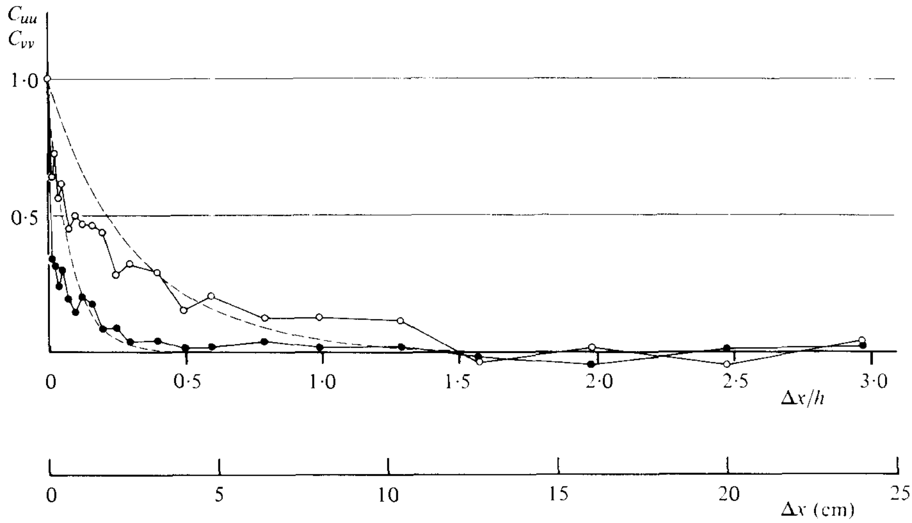

FIGURE 9. Space correlations of $C_{uu}(\Delta x, \tau = 0)$ and $C_{vv}(\Delta x, \tau = 0)$ at $y^+ = 38$. $C_{uu}(\Delta x, \tau = 0)$: ○—○, observed values; – – –, exp $(-\Delta x/L_u)$, $L_u = 2{\cdot}53$ cm. $C_{vv}(\Delta x, \tau = 0)$: ●—●, observed values; – – –, exp $(-\Delta x/L_v)$, $L_v = 0{\cdot}61$ cm.

in the inner layer are the same order of those in the outer layer obtained by Blackwelder & Kovasznay (1972), although the former is smaller than the latter.

Hence, it is considered that the small-eddy structure has been filtered out in the present data of the correlations due to the setting of the spanwise separation $\Delta z = 2$ mm when Δx is small. Indeed, this separation of Δz is comparatively large, since

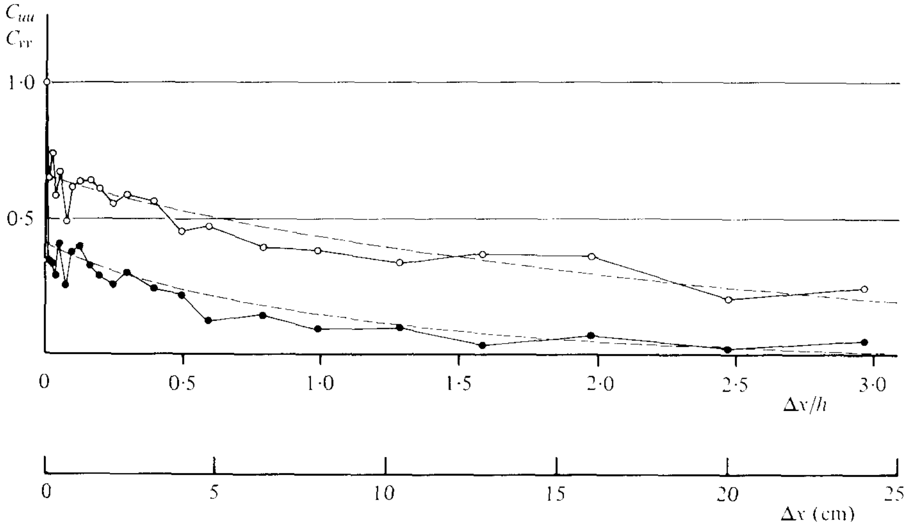

FIGURE 10. Space-time correlations of $C_{uu}(\Delta x, \tau_{\mathrm{opt}})$ and $C_{vv}(\Delta x, \tau_{\mathrm{opt}})$ with optimum delay at $y^+ = 38$. $C_{uu}(\Delta x, \tau_{\mathrm{opt}})$: ○—○, observed values; – – –, 0·64 exp $(-\Delta x/21{\cdot}3)$. $C_{vv}(\Delta x, \tau_{\mathrm{opt}})$: ●—●, observed values; – – –, 0·40 exp $(-\Delta x/7{\cdot}9)$.

$\Delta z^+ \equiv \Delta z U_*/\nu = 19$ corresponds to $\frac{1}{5}$ of the spacing $\bar{\lambda}^+ = 100$ between the low-speed streaks. Therefore, the values near the origin in figures 9 and 10 are unreliable for discussing the fine structure of turbulence. However, this is of little concern for the present purposes.

Next, figure 11 shows the variation of the iso-correlation curves of C_{uu}, while the time lag τ varies from $-0{\cdot}3$ s to $0{\cdot}3$ s. The large-eddy structure is convected downstream without any remarkable deformation during this time. This convection velocity U_c is $13{\cdot}2\ \mathrm{cm\,s^{-1}}$ as judged from figure 8, and it is nearly equal to the mean velocity $U = 13{\cdot}9\ \mathrm{cm\,s^{-1}}$ at $y_0/h = 0{\cdot}05$. From figure 11 (*d*), it is noticeable that the maximum correlation line fairly inclines downstream. This inclination angle toward the wall is 15–20° near the centre of the maximum iso-correlation, and it seems to become milder farther from the wall, which is in good agreement with the results of Blackwelder & Kovasznay (1972) and Brown & Thomas (1977).

Lastly, figure 12 shows an example of C_{uv} and C_{vu}. C_{uv} must be nearly equal to C_{vu} when the separation distance between the two probes is small, i.e.

$$|C_{uv}(\tau = 0)| \simeq |C_{vu}(\tau = 0)| \simeq R = (0{\cdot}3\text{–}0{\cdot}4).$$

However, there were some cases where $|C_{uv}| < |C_{vu}|$ appeared for the small positive values of Δx, as seen in figure 12 (*b*). Although this cause is quite unknown at present, it may be that, as regards the v component, the resolution of the V-type probe is worse than that of the X-type probe when the shear stress is large. From figure 7 and 12, it is understood that the spatial and time scales of the Reynolds stress are much smaller than those of the u component.

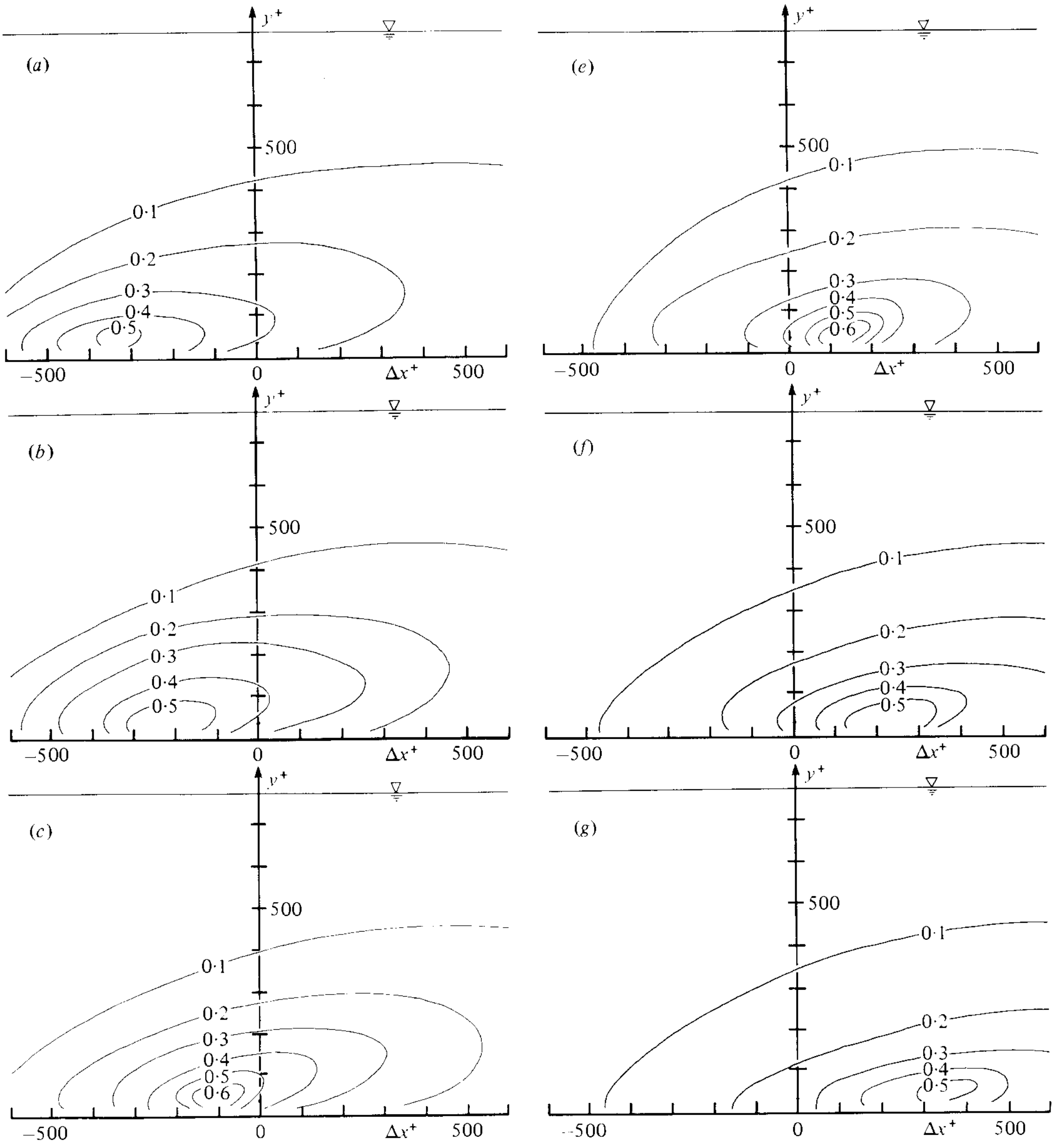

FIGURE 11 (*a*)–(*f*). For the caption see the next page.

4.3. *Eulerian time-correlations of bursting events by a new conditional sampling method*

In order to investigate Eulerian time-correlations of bursting events measured at one position, we have firstly sorted the velocity signals u, v and the Reynolds-stress signals $-uv$ into four quadrants of the u, v plane, as follows:

$$u_j(t) = u(t)\,I_j(t), \tag{17}$$

$$v_j(t) = v(t)\,I_j(t), \tag{18}$$

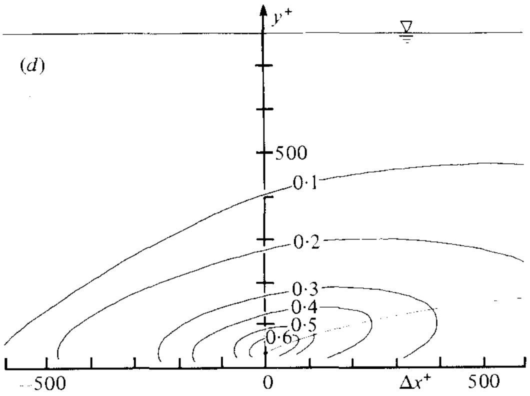

FIGURE 11. Iso-correlation contours of $C_{uu}(\Delta x, \tau)$ when the time lag τ varies from $-0·3$ s to $0·3$ s. (*a*) $\tau = -0·3$ s, (*b*) $\tau = -0·2$ s, (*c*) $\tau = -0·1$ s, (*d*) $\tau = 0·0$ s, (*e*) $\tau = 0·1$ s, (*f*) $\tau = 0·2$ s, (*g*) $\tau = 0·3$ s.

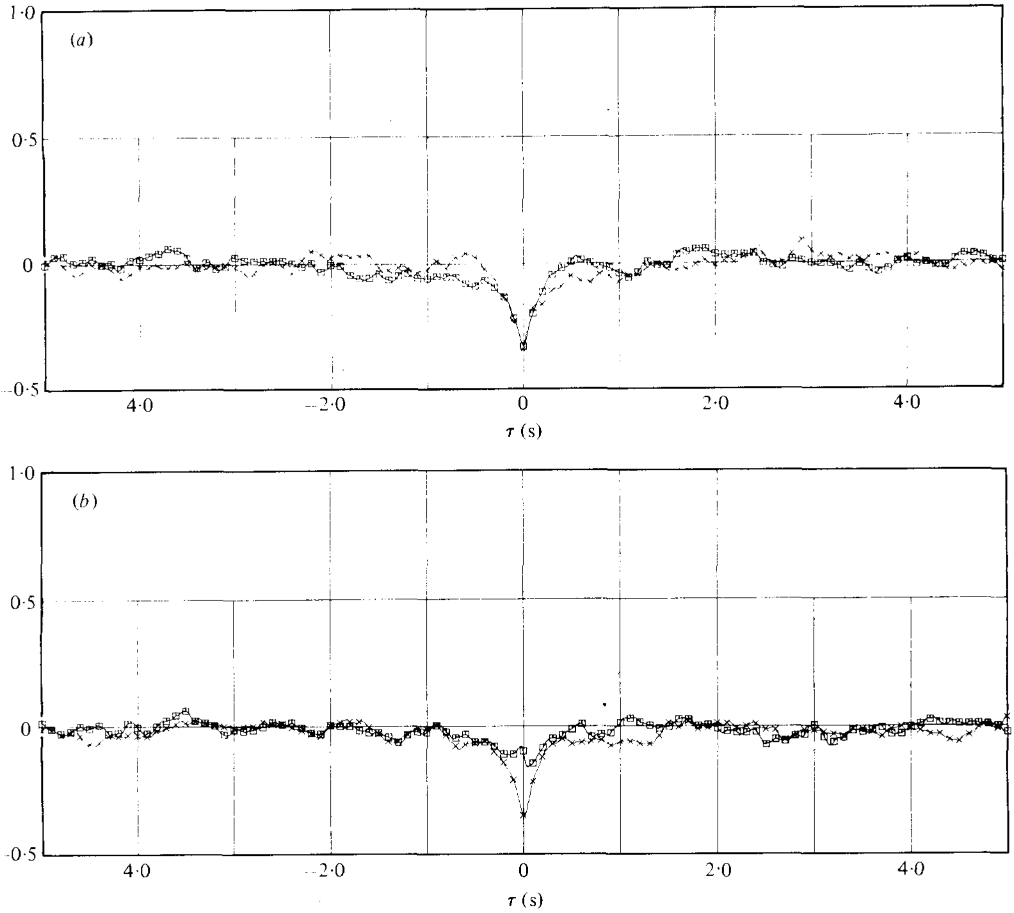

FIGURE 12. An example of space–time cross-correlations of u and v: –⊟–, $C_{uv}(\Delta x, \tau)$; –×–, $C_{vu}(\Delta x, \tau)$. $y_{\text{fix}} = 0·4$ cm, $y_{\text{mov}} = 0·7$ cm. (*a*) $\Delta x = -0·1$ cm, (*b*) $\Delta x = 0·1$ cm.

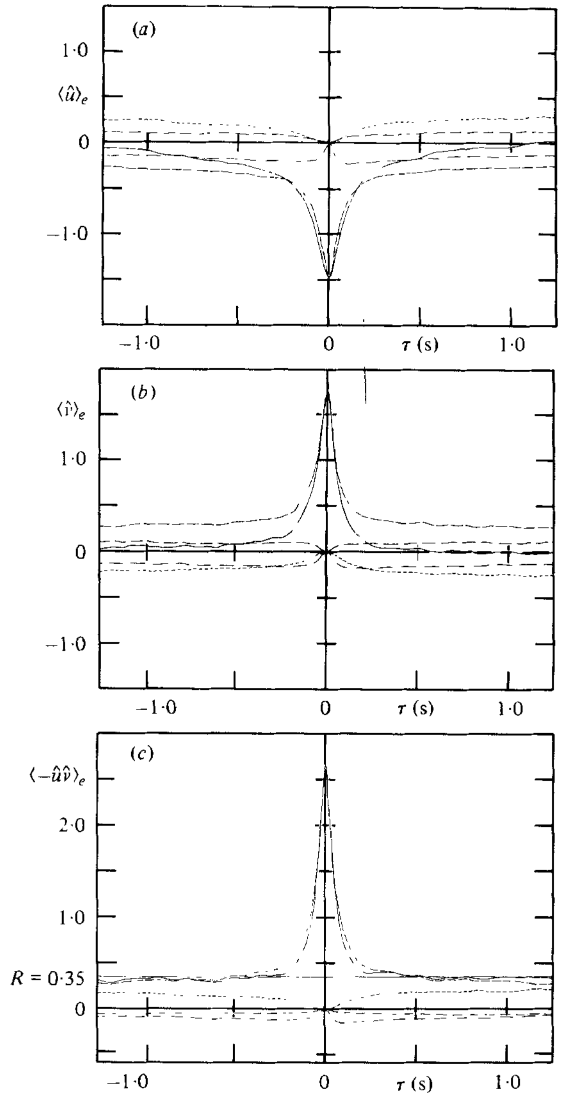

FIGURE 13. Conditionally averaged time correlations of u, v and $-uv$ when the ejections are detected at $y^+ = 38$; $y/h = 0{\cdot}05$.(a) $\langle \hat{u} \rangle_e(\tau)$, (b) $\langle \hat{v} \rangle_e(\tau)$, (c) $\langle -\hat{u}\hat{v} \rangle_e(\tau)$. — — —, ejection; - - - - -, sweep; —·—, outward interaction; —··—, inward interaction; ——, total events.

$$(-uv)_j\,(t) = (-uv)\,(t)\,I_j(t), \tag{19}$$

where $j = 1, 2, 3$ and 4 (see (5)–(8)).

Next, by using the new conditional averaging method of (9) and (10), the Eulerian time correlations $\langle \hat{u} \rangle_e(\tau)$, $\langle \hat{v} \rangle_e(\tau)$, $\langle -\hat{u}\hat{v} \rangle_e(\tau)$ and $\langle \hat{u} \rangle_s(\tau)$, $\langle \hat{v} \rangle_s(\tau)$, $\langle -\hat{u}\hat{v} \rangle_s(\tau)$ of each bursting event were obtained at $y_0^+ = y_1^+ = 38$, respectively. Figures 13 and 14 show these results, in which the thirteen-times ensemble averaging, i.e. the data size $N = 13 \times 10000$, was carried out in order to enhance the accuracy. The solid line in these figures indicates the total contributions from all events, that is, the conditional

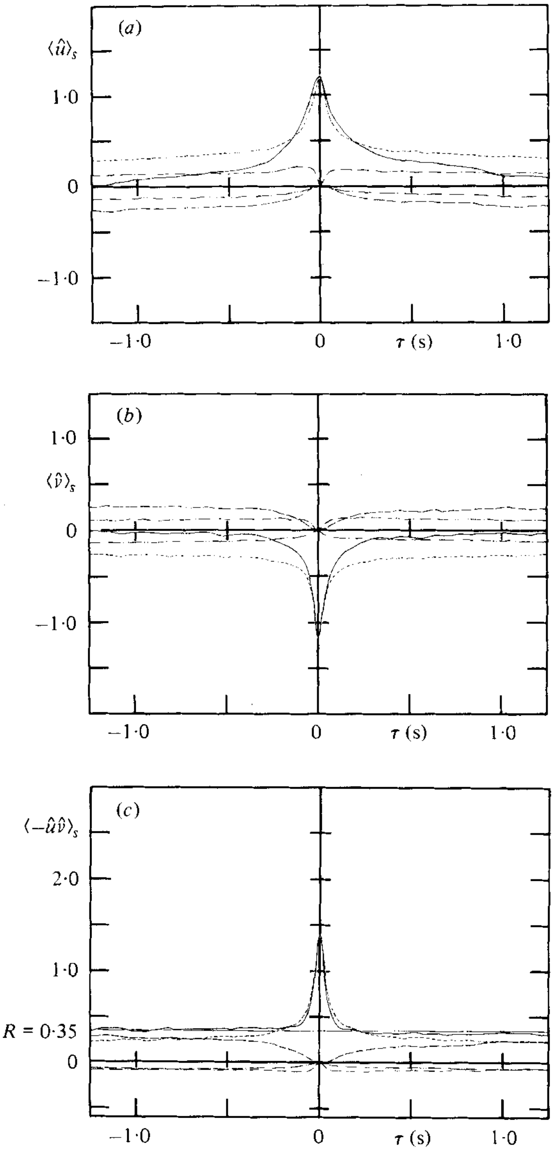

FIGURE 14. Conditionally averaged time correlations of u, v and $-uv$ when the sweeps are detected at $y^+ = 38$. (a) $\langle \hat{u} \rangle_s(\tau)$, (b) $\langle \hat{v} \rangle_s(\tau)$, (c) $\langle -\hat{u}\hat{v} \rangle_s(\tau)$. Notation as in figure 13.

time-correlation of $\hat{u}$, $\hat{v}$ or $(-\hat{u}\hat{v})$, itself. Of course, $\langle \hat{u} \rangle_e \leqslant 0, \langle \hat{v} \rangle_e \geqslant 0$ and $\langle -\hat{u}\hat{v} \rangle_e \geqslant R$ during the ejection phase (figure 13), in which the ejection motion is detected at $y_0^+ = 38$, while $\langle \hat{u} \rangle_s \geqslant 0, \langle \hat{v} \rangle_s \leqslant 0$ and $\langle -\hat{u}\hat{v} \rangle_s \geqslant R$ during the sweep phase (figure 14). Obviously, the ejections are stronger than the sweeps, which is in good agreement with the previous results that $RS_2 > RS_4$ in figure 6. Also, the peak values of $\langle \hat{u} \rangle$, $\langle \hat{v} \rangle$ and $\langle -\hat{u}\hat{v} \rangle$ are comparable with the previous results which were obtained from the different detecting method with a threshold level H by Lu & Willmarth (1973), Nakagawa & Nezu (1978) and Nezu & Nakagawa (1981).

Since the conditional averages are asymmetric in regard to $\tau = 0$, the time scale

Ejections	$\mathcal{T}_{-}U_{\max}/h$ $(\tau < 0)$	$\mathcal{T}_{+}U_{\max}/h$ $(\tau > 0)$	Mean value $\mathcal{T} \equiv \frac{1}{2}(\mathcal{T}_{-}+\mathcal{T}_{+})$
$\langle\hat{u}\rangle_e$	0·67	0·50	0·59
$\langle\hat{v}\rangle_e$	0·34	0·22	0·28
$\langle-\hat{u}\hat{v}\rangle_e$	0·16	0·18	0·17
Sweeps			
$\langle\hat{u}\rangle_s$	0·68	0·85	0·77
$\langle\hat{v}\rangle_s$	0·28	0·36	0·32
$\langle-\hat{u}\hat{v}\rangle_s$	0·14	0·10	0·12

TABLE 2. Time scales $\mathcal{T}$ of the ejection and sweep motions.

$\mathcal{T}$ of the ejections and sweeps is defined separately for $\tau < 0$ and $\tau > 0$, in a similar way to (15) and (16), as follows:

$$\mathcal{T}_{\langle u\rangle_e^-} = \int_{\tau^-}^{0} \frac{\langle\hat{u}\rangle_e(\tau)}{\langle\hat{u}\rangle_e(0)}\,d\tau, \quad \mathcal{T}_{\langle u\rangle_e^+} = \int_{0}^{\tau^+} \frac{\langle\hat{u}\rangle_e(\tau)}{\langle\hat{u}\rangle_e(0)}\,d\tau \tag{20}$$

where τ^- and τ^+ are the time lag up to the zero-cross of $\langle\hat{u}\rangle_e\,(\tau)$ for $\tau < 0$ and $\tau > 0$, respectively. The time scales of $\langle\hat{v}\rangle_e$, $\langle\hat{u}\rangle_s$ and $\langle\hat{v}\rangle_s$ are also defined in the same manner as (20). The time scales of the conditionally averaged Reynolds stress $\langle-\hat{u}\hat{v}\rangle_e$ and $\langle-\hat{u}\hat{v}\rangle_s$ are defined as follows:

$$\mathcal{T}_{\langle -uv\rangle^-} = \int_{\tau^-}^{0} \frac{\langle-\hat{u}\hat{v}\rangle(\tau)-R}{\langle-\hat{u}\hat{v}\rangle(0)-R}\,d\tau, \quad \mathcal{T}_{\langle -uv\rangle^+} = \int_{0}^{\tau^+} \frac{\langle-\hat{u}\hat{v}\rangle(\tau)-R}{\langle-\hat{u}\hat{v}\rangle(0)-R}\,d\tau. \tag{21}$$

The time scales evaluated from the above equations are described in table 2. It is obvious that the time scale of the velocity component $\langle u\rangle$ is largest, while the time scale of the Reynolds stress $\langle -uv\rangle$ is smallest, for both ejections and sweeps. This confirms again that the instantaneous Reynolds stress shows an intermittent or pulse-like behaviour, which has been already revealed both theoretically and experimentally by the authors (1977*a*, 1978). It is suggested that the momentum transfer in the vertical direction (y) may be done in a short time, since $\mathcal{T}_{\langle v\rangle} < \mathcal{T}_{\langle u\rangle}$. From figures 13, 14 and table 2, it can be generally concluded that the ejection motion occurs more violently and shortly than does the sweep motion, which coincides well with the previous visual observations (e.g. Corino & Brodkey 1969).

Next, for the u and v components, $\mathcal{T}_{-} > \mathcal{T}_{+}$ during the ejection phase, while $\mathcal{T}_{-} < \mathcal{T}_{+}$ during the sweep phase. This suggests strongly that the ejection motion occurs slowly and then decays rapidly, while the sweep motion occurs rapidly and then decays slowly, which is again consistent with visual observations (e.g. Corino & Brodkey 1969 or Grass 1971). Consequently, in the Eulerian observation the transition from the ejection to sweep motions occurs more rapidly than does the transition from the sweep to ejection motions. This coincides well with the results obtained from the other conditional analysis, i.e. VITA-method, by Blackwelder & Kaplan (1976), and also the renewal model by Nakagawa & Nezu (1978). On the other hand, for the Reynolds-stress signals, the opposite tendency appears, although the difference between $\mathcal{T}_{-}$ and $\mathcal{T}_{+}$ is small in both ejections and sweeps. This may be due to a greater contribution of the sweep event to $\mathcal{T}_{+}$ of the ejection phase (see figure 13*c*), and also of the ejection event to $\mathcal{T}_{-}$ of the sweep phase (see figure 14*c*), since the transition from the ejection to sweep motions occurs more rapidly.

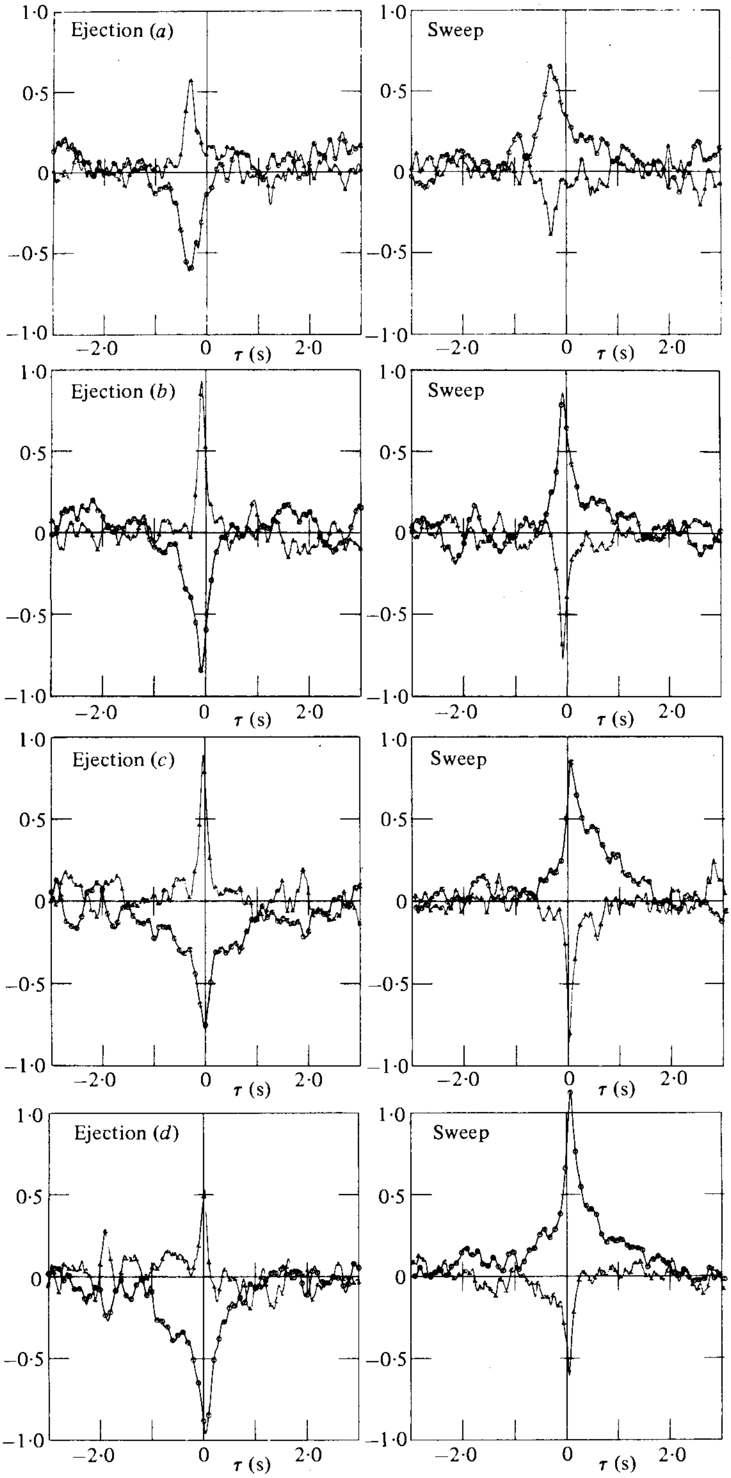

FIGURE 15 (*a*)–(*d*). For the caption see the next page.

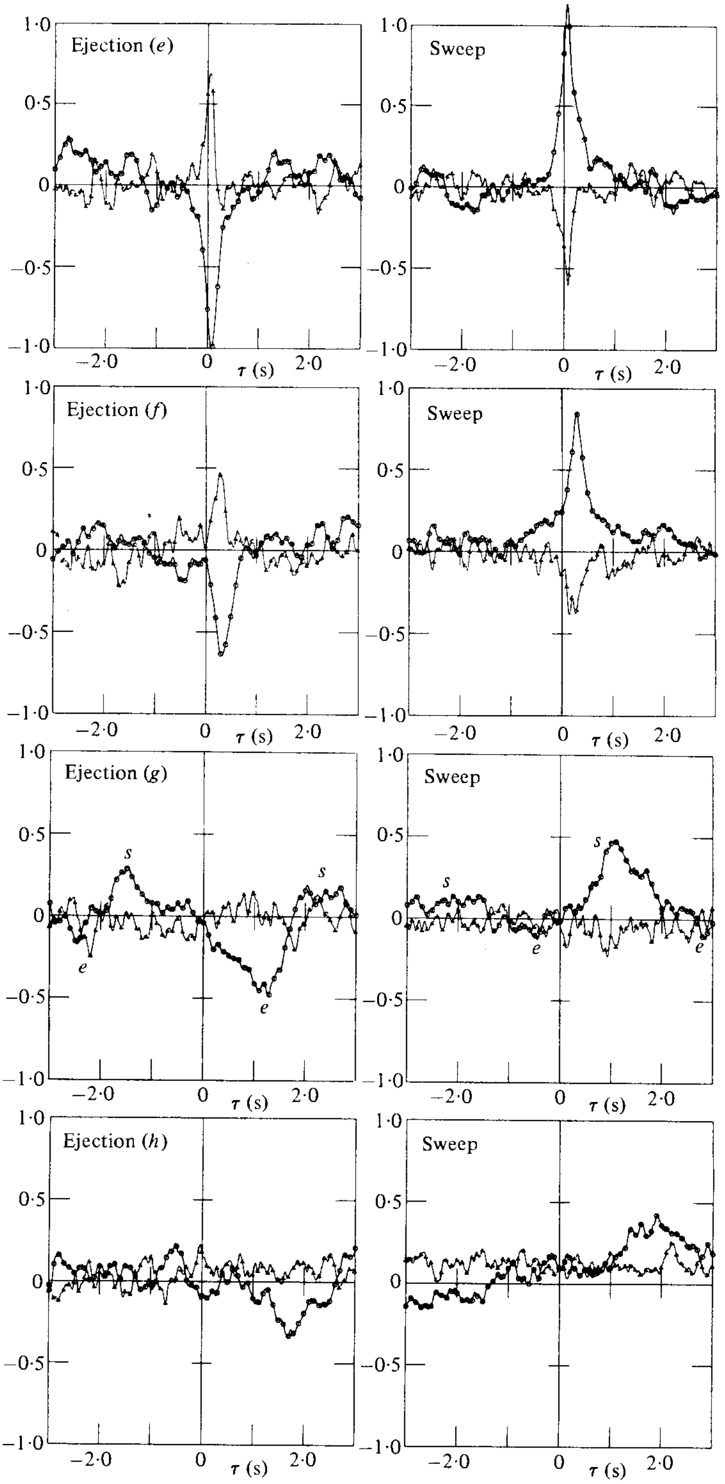

FIGURE 15. Conditionally averaged space–time correlations $\langle \hat{u} \rangle$ $(\Delta x, \tau)$ and $\langle \hat{v} \rangle$ $(\Delta x, \tau)$ in the wall region (i.e. at $y^+_{\text{mov}} = 38$) when the ejection motion or the sweep motion occurs at the fixed probe ($y^+_{\text{fix}} = 38$). (*a*) $\Delta x = -4{\cdot}0$ cm, (*b*) $\Delta x = -1{\cdot}0$ cm, (*c*) $\Delta x = -0{\cdot}1$ cm, (*d*) $\Delta x = 0{\cdot}1$ cm, (*e*) $\Delta x = 1{\cdot}0$ cm, (*f*) $\Delta x = 4{\cdot}0$ cm, (*g*) $\Delta x = 16{\cdot}0$ cm, (*h*) $\Delta x = 32{\cdot}0$ cm. ○—○, $\langle \hat{u} \rangle$ $(\Delta x, \tau)$; △—△, $\langle \hat{v} \rangle$ $(\Delta x, \tau)$.

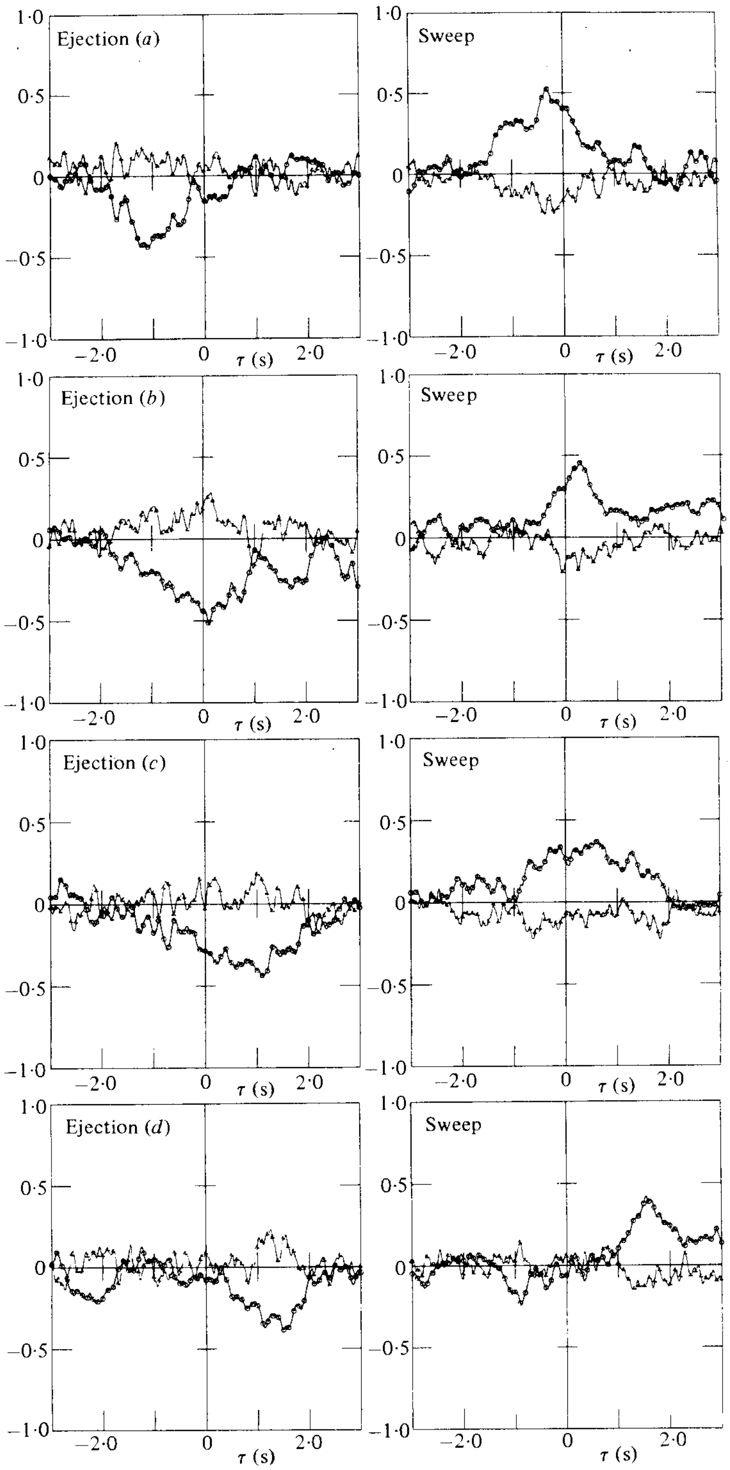

FIGURE 16. Conditionally averaged space–time correlations $\langle \hat{u} \rangle (\Delta x, \tau)$ and $\langle \hat{v} \rangle (\Delta x, \tau)$ in the equilibrium region (i.e. at $y_{\mathrm{mov}}/h = 0{\cdot}3$). (a) $\Delta x = 0{\cdot}0$ cm, (b) $\Delta x = 8{\cdot}0$ cm, (c) $\Delta x = 16{\cdot}0$ cm, (d) $\Delta x = 32{\cdot}0$ cm. Notation as in figure 15.

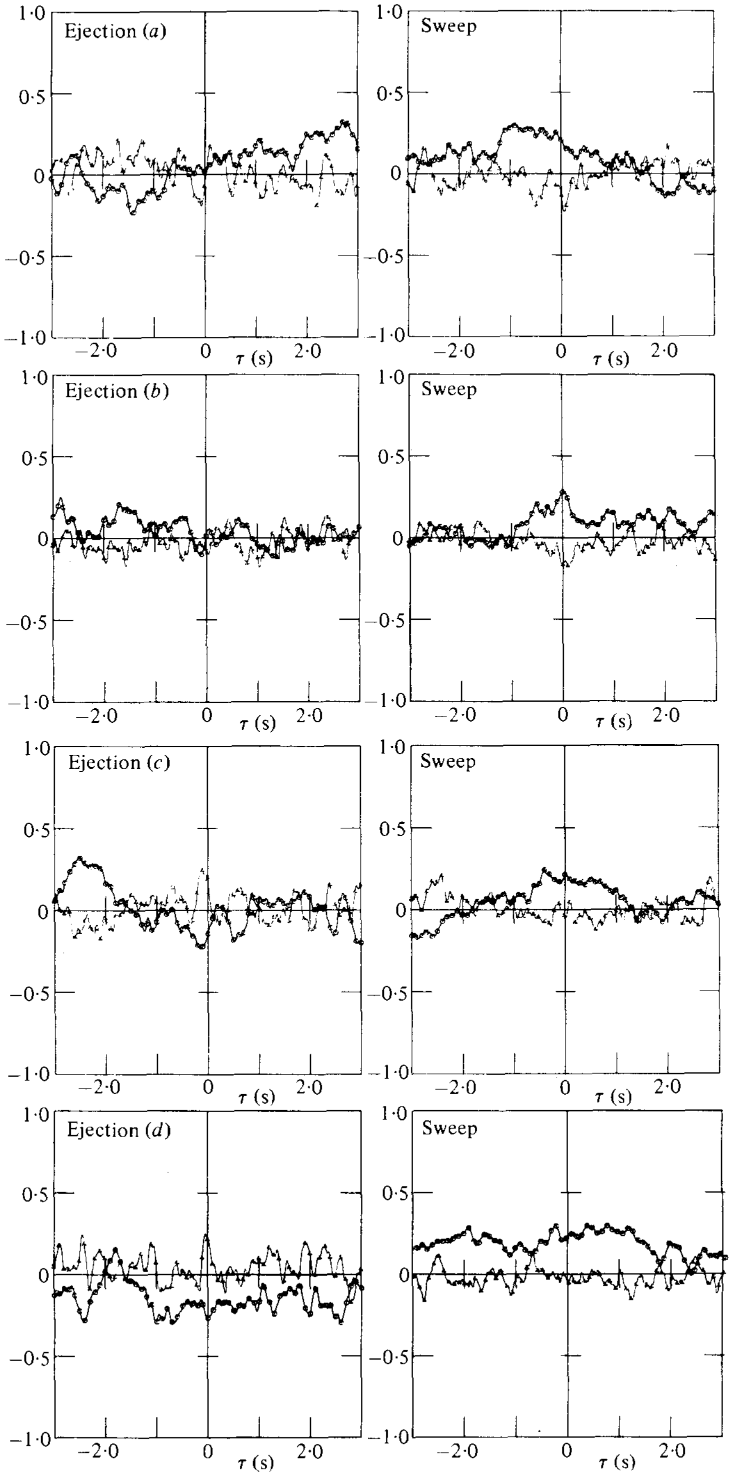

FIGURE 17. Conditionally averaged space–time correlations $\langle \hat{u} \rangle$ $(\Delta x, \tau)$ and $\langle \hat{v} \rangle$ $(\Delta x, \tau)$ in the free-surface region (i.e. at $y_{\mathrm{mov}}/h = 0{\cdot}74$). (*a*) $\Delta x = 0{\cdot}0$ cm, (*b*) $\Delta x = 8{\cdot}0$ cm, (*c*) $\Delta x = 16{\cdot}0$ cm, (*d*) $\Delta x = 32{\cdot}0$ cm. Notation as in figure 15.

Finally, the results of the present quadrant analysis are consistent with those obtained from the pattern-recognition technique by Wallace *et al.* (1977). However, the detailed comparison cannot be done, since the former has the real time axis τ, while the latter has the time axis normalized by each bursting period. It should be noticed that the inward-interaction event coexists up to near the origin $\tau = 0$ during the ejection phase (see figure 13), while the outward-interaction event coexists during the sweep phase (see figure 14). This has been already inferred theoretically by Nakagawa & Nezu (1977*a*).

4.4. *Space–time structure of bursting motions by the present conditional analysis*

If the signals $\hat{u}_{\mathrm{mov}}$ and $\hat{v}_{\mathrm{mov}}$ from the movable probe are substituted for q in (9) or (10), we can obtain the space–time structures $\langle\hat{u}\rangle(\tau)$ and $\langle\hat{v}\rangle(\tau)$ when the ejection motion or the sweep motion occurs at the fixed probe ($y^+_{\mathrm{fix}} = 38$). Figures 15–17 show several examples of such data described by the X–Y plotter.

Figure 15 shows some results obtained in the wall region, i.e. at $y^+_{\mathrm{mov}} = y^+_{\mathrm{fix}} = 38$, in which the separation Δx varies from $-0{\cdot}5h$ up to $4h$. The smaller the separation $|\Delta x|$ is, the larger the peaks of $\langle\hat{u}\rangle$ and $\langle\hat{v}\rangle$ patterns become. Obviously, the averaged patterns of recognized u and v are approximately 180° out of phase, and this agrees with the results by Wallace *et al.* (1977). Of course, these patterns for the very small separation (figure 15(*c*), (*d*)) should coincide well with the patterns for $\Delta x = 0$, as shown in figures 13 and 14.

The peaks of $\langle\hat{u}\rangle$ and $\langle\hat{v}\rangle$ decrease gradually and also become flatter, with an increase of Δx. However, the $\langle\hat{v}\rangle$ pattern for the larger separation (see figure 15(*h*)) may show only the ripple scattering, since the v-component decayed more rapidly and also its probe resolution was worse than the u-component, as mentioned previously. It is seen most clearly in figure 15(*g*) that the cyclic pattern of the ejection–sweep–ejection motions appears on an average, as observed visually. Furthermore, the transition from the ejection (*e*) to sweep (*s*) motions occurs more rapidly than the reverse transition $(s) \rightarrow (e)$, which is considered to be one of the most essential characteristics of the bursting phenomenon.

Figures 16 and 17 show some typical results in the equilibrium and the free-surface regions, respectively. Although the properties of the $\langle\hat{u}\rangle$ and $\langle\hat{v}\rangle$ patterns are generally similar to those shown in figure 15, their peaks appear at the negative time lag when $\Delta x = 0$. This means that the phase of bursting motions in the region farther from the wall goes ahead of that at the detecting position $y^+_{\mathrm{fix}} = 38$ near the wall. Recently, Kreplin & Eckelmann (1979) measured the conventional space–time correlations of the streamwise and spanwise fluctuations of the velocity and the velocity gradient at the wall in an oil channel flow, and they concluded that the phase of the perturbations near the buffer layer goes ahead of that in the viscous sublayer. Such a result is consistent with the present result.

Another striking feature is that the bursting motion occurring in the wall region extends up to the free-surface region (see figure 17, where $y_{\mathrm{mov}}/h = 0{\cdot}74$), although the $\langle\hat{v}\rangle$ pattern may have comparatively large errors. Indeed, some examples where the states of $\langle\hat{u}\rangle < 0$ (ejection phase) and $\langle\hat{u}\rangle > 0$ (sweep phase) continue stably and longer than the bursting period, have been obtained for the larger separation $\Delta x/h \geqslant 3$ in the free-surface region, as seen in figure 17 (*d*). Such a feature is also seen in the conditionally averaged data of Grass (1971). This suggests that there may exist an interrelation

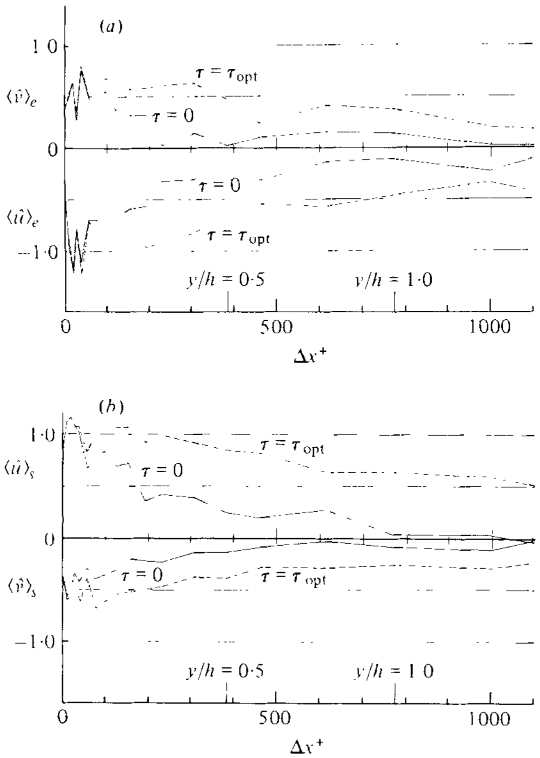

FIGURE 18. Space structures of $\langle \hat{u}\rangle$ $(\Delta x, \tau = 0)$, $\langle \hat{v}\rangle$ $(\Delta x, \tau = 0)$ and $\langle \hat{u}\rangle$ $(\Delta x, \tau_{\mathrm{opt}})$, $\langle \hat{v}\rangle$ $(\Delta x, \tau_{\mathrm{opt}})$ of the ejection and sweep motions observed at $y^+ = 38$. (*a*) Ejection motion, (*b*) sweep motion. ——, $\tau = 0$; – – –, $\tau = \tau_{\mathrm{opt}}$.

between the bursting motion and the stable high-speed and low-speed streaks or the boiling phenomena which were observed on the free surface of a river by Kinoshita (1967) and Jackson (1976).

Next, figure 18 shows the space structures of $\langle \hat{u}\rangle(\Delta x)$ and $\langle \hat{v}\rangle(\Delta x)$ of the ejection and sweep motions at $y^+ = 38$, for $\tau = 0$ by the solid line and $\tau = \tau_{\mathrm{opt}}$ by the broken line at which both $\langle \hat{u}\rangle(\Delta x)$ and $\langle \hat{v}\rangle(\Delta x)$ attain the peaks. The results in the case of $\Delta x < 0$ were also nearly the same as figure 18. These characteristics are roughly similar to those of the conventional long-time averaging structures in figures 9 and 10. It is easily understood that the u component keeps its coherent structure over a longer distance than does the v component. The same is also true for the sweeps compared with the ejections. In order to evaluate quantitatively the spatial scales $\mathscr{L}$ of the ejections and sweeps for $\tau = 0$, we define the following in the same manner as (20):

$$\mathscr{L}_{\langle u\rangle_e^-} = \int_{\Delta x-}^{0} \frac{\langle \hat{u}\rangle_e(\Delta x)}{\langle \hat{u}\rangle_e(0)}\, d(\Delta x), \quad \mathscr{L}_{\langle u\rangle_e^+} = \int_{0}^{\Delta x+} \frac{\langle \hat{u}\rangle_e(\Delta x)}{\langle \hat{u}\rangle_e(0)}\, d(\Delta x), \quad \text{etc.} \tag{22}$$

The results evaluated from (22) are described in table 3, separately for $\Delta x < 0$ and $\Delta x > 0$. If the bursting motions are convected downstream in the frozen-turbulence manner, we can obtain

$$\mathscr{L}_{\langle u\rangle_e^-} = U_{c,\langle u\rangle_e} \times \mathscr{T}_{\langle u\rangle_e^+}, \quad \mathscr{L}_{\langle u\rangle_e^+} = U_{c,\langle u\rangle_e} \times \mathscr{T}_{\langle u\rangle_e^-}, \quad \text{etc.} \tag{23}$$

	$\mathscr{L}_-/h$ ($\Delta x < 0$)	$\mathscr{L}_+/h$ ($\Delta x > 0$)	Mean value $\mathscr{L} = \frac{1}{2}(\mathscr{L}_- + \mathscr{L}_+)$
Ejections			
$\langle \hat{u} \rangle_e$	0·24	0·28	0·26
	(0·28)	(0·38)	(0·33)
$\langle \hat{v} \rangle_e$	0·09	0·13	0·11
	(0·13)	(0·20)	(0·16)
Sweeps			
$\langle \hat{u} \rangle_s$	0·41	0·33	0·37
	(0·59)	(0·47)	(0·53)
$\langle \hat{v} \rangle_s$	0·17	0·13	0·15
	(0·24)	(0·18)	(0·21)
Mean eddy			
L_u/h	—	—	0·31
L_v/h	—	—	0·08

TABLE 3. Spatial scales $\mathscr{L}$ of the ejection and sweep motions. The value in the parentheses is equal to (the time-scale) × (the convection velocity), i.e. $\mathscr{T} \times U_c$. (See equation (23).)

Since the time scales $\mathscr{T}$ have been given in table 2, and also the convection velocity U_c of each bursting motion is easily obtained as described in the next section, the spatial scales of (23) can be evaluated and are indicated in the parentheses of table 3. The data from (22) are somewhat smaller than the data from (23), which limits the perfectly-frozen-turbulence concept. However, this inequality may be also quite possible due to the inaccuracy of the profiles near the origin in figure 18, which were caused by the spanwise separation Δz, as pointed out previously.

The characteristics of the two are similar in the following respects.

(i) The spatial scale of u is larger than that of v.

(ii) The spatial scale of the sweeps is larger than that of the ejections.

(iii) The spatial scale of the ejections extends more widely downstream rather than upstream, i.e. $\mathscr{L}_- < \mathscr{L}_+$, and vice versa for the sweeps.

(iv) The spatial scales $\mathscr{L}$ of the bursting motions coincide roughly with the mean eddy scales L_u and L_v given by (15) and (16).

These characteristics infer that the bursting motion is a kind of large-eddy structure and it is convected very coherently, i.e. with a frozen-turbulence-like pattern.

Furthermore, figure 19 shows the spatial patterns of $\langle \hat{u} \rangle_e$ and $\langle \hat{u} \rangle_s$ for $\tau = 0$ at each different position y_{mov}. Although there is some scatter in these data, the peak positions (of course, $\langle \hat{u} \rangle$ is negative and positive for the ejection and sweep phases, respectively) shift in the downstream with an increase of the height y. Thus, $\langle \hat{u} \rangle (\Delta x, y)$ is normalized by $\langle \hat{u} \rangle (\Delta x = 0, y_{\mathrm{fix}})$ instead of $\langle \hat{u} \rangle (\Delta x = 0, y)$, and the following characteristic-scale $\mathscr{L}$ is defined here:

$$\mathscr{L}_{\langle u \rangle_e}(y) = \frac{1}{2} \int_{\Delta x-}^{\Delta x+} \frac{\langle \hat{u} \rangle_e (\Delta x, y)}{\langle \hat{u} \rangle_e (\Delta x = 0, y_{\mathrm{fix}})} d(\Delta x), \quad \text{etc.,} \tag{24}$$

where Δx_- and Δx_+ are the zero-crossing positions, between which there exists a peak of $\langle \hat{u} \rangle$.

Of course, $\mathscr{L}(y_{\mathrm{fix}}) = \frac{1}{2}(\mathscr{L}_- + \mathscr{L}_+)$ in table 3. $\mathscr{L}$ may be favourably called 'the influence scale of the bursting motion', due to its definition of (24), i.e. $\mathscr{L} =$ (strength of the influence) × (distance over which the influence appears).

Figure 20 shows the influence scale $\mathscr{L}$ of the bursting motions, in which the data at

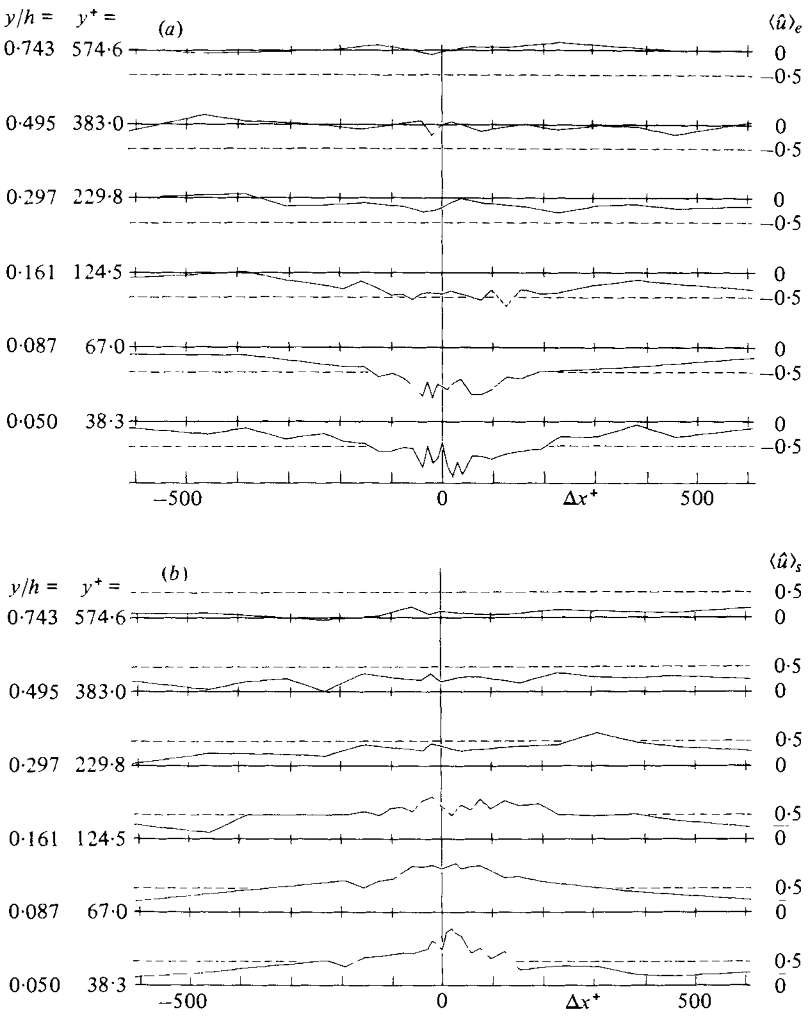

FIGURE 19. Spatial patterns of $\langle \hat{u}\rangle_e(\Delta x)$ and $\langle \hat{u}\rangle_s(\Delta x)$ for $\tau = 0$ obtained at each different position, y_{mov}. (*a*) Ejection motion, (*b*) sweep motion.

$y/h = 0{\cdot}74$ could not be obtained because Δx_+ was out of the measurement range, i.e. $\Delta x_+ > 4h$. The relationship that $\mathscr{L}_{\langle u\rangle_s} > \mathscr{L}_{\langle u\rangle_e} > \mathscr{L}_{\langle v\rangle_s} > \mathscr{L}_{\langle v\rangle_e}$ is seen again. A noticeable tendency is that the influence scale increases with an increase of y^+ in the wall region ($y^+ \leqslant 100$), while it decreases with y^+ in the equilibrium region or the outer layer. This suggests that the bursting motions occurring near the buffer layer develop up to the edge of the wall region and then decay gradually in the outer layer, which is in many respects consistent with visual observation by Offen & Kline (1975).

4.5. *Convection process of the bursting motions*

Figures 21 and 22 show the spatial iso-patterns of the $\langle \hat{u}\rangle$ and $\langle \hat{v}\rangle$ components, respectively, at the instant when the ejection or sweep motions occur at $y^+ = 38$. To discriminate easily, the negative regions of $\langle \hat{u}\rangle$ and $\langle \hat{v}\rangle$ are hatched. Evidently, the spatial pattern of $\langle \hat{u}\rangle$ is fairly inclined downstream, similar to the large eddy in figure 11.

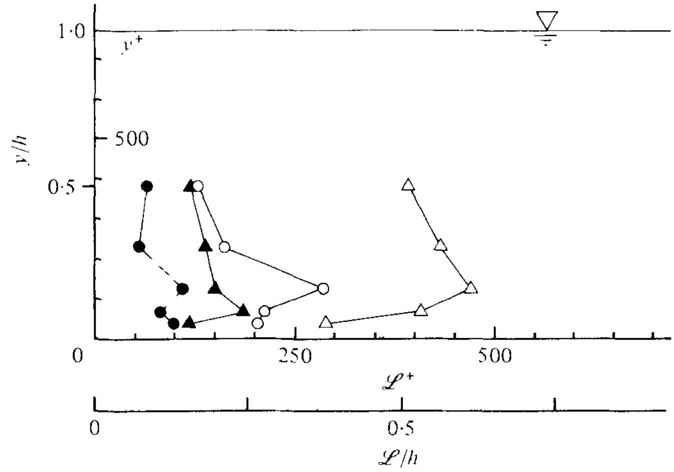

FIGURE 20. Influence scale $\mathscr{L}$ of the bursting motions. ○, $\langle\hat{u}\rangle_e$; △, $\langle\hat{u}\rangle_s$; ●, $\langle\hat{v}\rangle_e$; ▲, $\langle\hat{v}\rangle_s$.

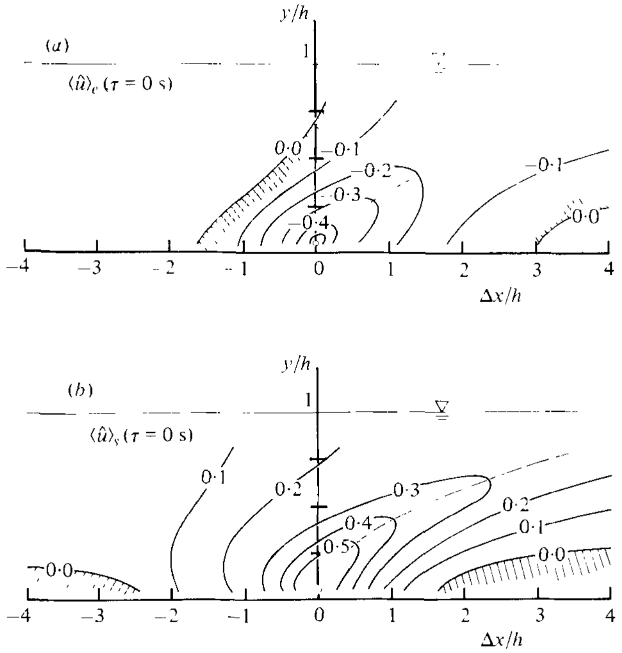

FIGURE 21. Spatial iso-patterns of $\langle\hat{u}\rangle$ at the instant when the ejection and sweep motions occur at $y^+ = 38$. (*a*) Ejection motion, (*b*) sweep motion. The hatched region denotes negative values.

According to the detailed examination in the region $|\Delta x| \leqslant h$ where the measurement has been densely performed, the inclination angles of the iso-lines of $\langle\hat{u}\rangle_e$ and $\langle\hat{u}\rangle_s$ toward the wall are both about 20–25° near the detecting probe. Then, they become milder as they go farther from the wall, that is, about 10° near the middle flow depth. On the other hand, the iso-patterns of $\langle\hat{v}\rangle$ do not show any conspicuous inclination characteristic in the wall region at least, but $\langle\hat{v}\rangle$ has the strongest correlation in the vertical

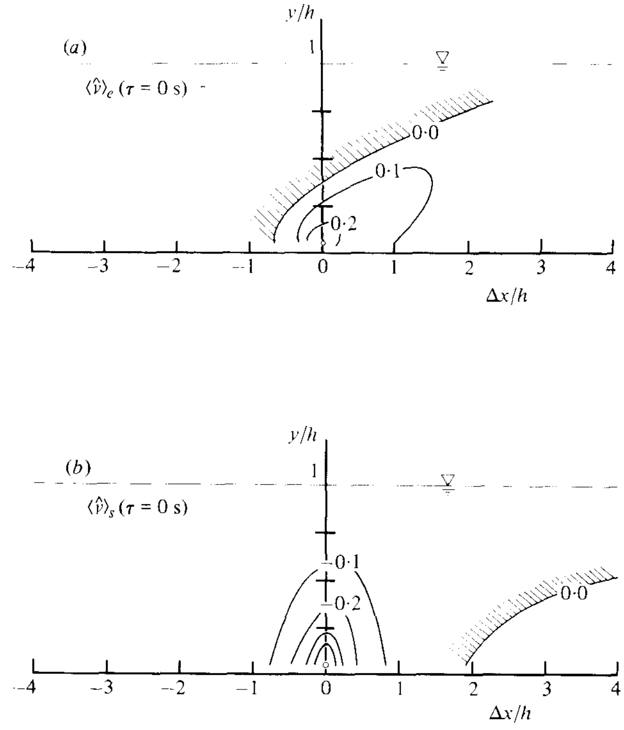

FIGURE 22. Spatial iso-patterns of $\langle\hat{v}\rangle$ at the instant when the ejection and sweep motions occur at $y^+ = 38$. (*a*) Ejection motion, (*b*) sweep motion. The hatched region denotes negative values.

direction. Comparing the difference of these inclinations between the $\langle\hat{u}\rangle$ and $\langle\hat{v}\rangle$ patterns, the v fluctuation involved in the ejection and sweep motions seems to decay more rapidly than does the u fluctuation, since the former is apt to be more influenced by the velocity shear. Consequently, the scale of the $\langle\hat{v}\rangle$ pattern may become smaller than that of the $\langle\hat{u}\rangle$ pattern, as mentioned previously. By comparison between the ejection and sweep motions, the spatial-scale characteristics of the bursting motions given in the previous section are clearly understood again.

Next, figure 23 shows the iso-patterns of $\langle\hat{u}\rangle$ at one second after the occurrence of the bursting motion at the detecting probe. This elapsing time $\tau U_{\max}/h = 2{\cdot}6$ corresponds to the bursting passing-period $T_B U_{\max}/h = (1{\cdot}5\text{–}3{\cdot}0)$ which was evaluated in open-channel flows by Nakagawa & Nezu (1978). By comparison with figure 21, the most striking feature is that the $\langle\hat{u}\rangle$ pattern of the bursting motions is surely convected downstream without its remarkable deformation, namely in the frozen-turbulence-like manner. This is considered to be caused by the following: (1) The Lagrangian lifetime T_l of the u fluctuation involved in the bursting motions is much larger than the bursting passing-period T_B. Since the bursting motion is a kind of large coherent-eddy, $T_l U_{\max}/h$ may be roughly larger than 10, as inferred from the result by Blackwelder & Kovasznay (1972). (2) Its convection velocity in the vertical direction, which is comparable to v', is much smaller by one order of magnitude than the convection velocity U_c in the streamwise direction, that is, $v'/U_c \simeq 0{\cdot}1$. This result has been confirmed by Eckelmann (1974) and recently by Kreplin & Eckelmann (1979).

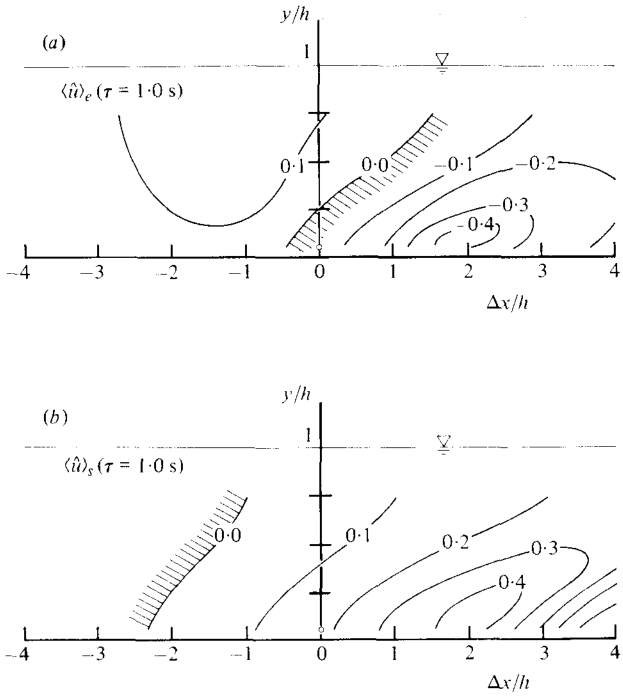

FIGURE 23. Spatial iso-patterns of $\langle \hat{u} \rangle$ at the time when $\tau U_{\max}/h = 2{\cdot}6$ passed after the occurrence of the bursting motions at the detecting probe. (*a*) Ejection motion, (*b*) sweep motion. The hatched region denotes negative values.

Lastly, figures 24 and 25 show the optimum delay time τ_{opt} of $\langle \hat{u} \rangle$ and $\langle \hat{v} \rangle$ against the separation Δx, respectively. Although the data in the region far from the wall scatter each other due to the flatter profile of $\langle \hat{u} \rangle (\tau)$ and $\langle \hat{v} \rangle (\tau)$, it is noticeable that the convection velocity of the sweep motion is a little larger than that of the ejection motion. The average of the two becomes nearly equal to the convection velocity of a large eddy observed by the conventional long-time average of 4·2. In particular, the convection velocity of the ejection motion becomes nearly equal to $U_{c,\langle u \rangle_e}/U \simeq 0{\cdot}8$, which agrees well with the result by Lu & Willmarth (1973). Another outstanding feature is that the phase of the $\langle \hat{u} \rangle$ pattern far from the wall goes ahead of that near the wall (compare figure 24 (*a*) with (*c*)), while the $\langle \hat{v} \rangle$ pattern has nearly the same phase at least up to the outside of the wall region (see figure 25). This explains again the inclination characteristics of the bursting motions.

4.6. *Spanwise spatial structure of the bursting motions*

It is recognized sufficiently by many visual observations (e.g. Kline and his co-workers 1967, 1971, 1975) that the spanwise spatial structure in the wall region consists of the high-speed and low-speed streaks, whose spacing $\lambda^+ \equiv \lambda U_*/\nu$ is nearly constant, *viz.* $\lambda^+ \simeq 100$. Our earlier visual study (Nakagawa & Nezu 1977*b*) of an open-channel flow has also found that, although there exists clearly a streaky structure of $\lambda^+ \simeq 100$ in the wall region (see figure 26, which is cited from our visual observations), the streaky structure becomes gradually indistinct outside the wall region and its spacing λ^+

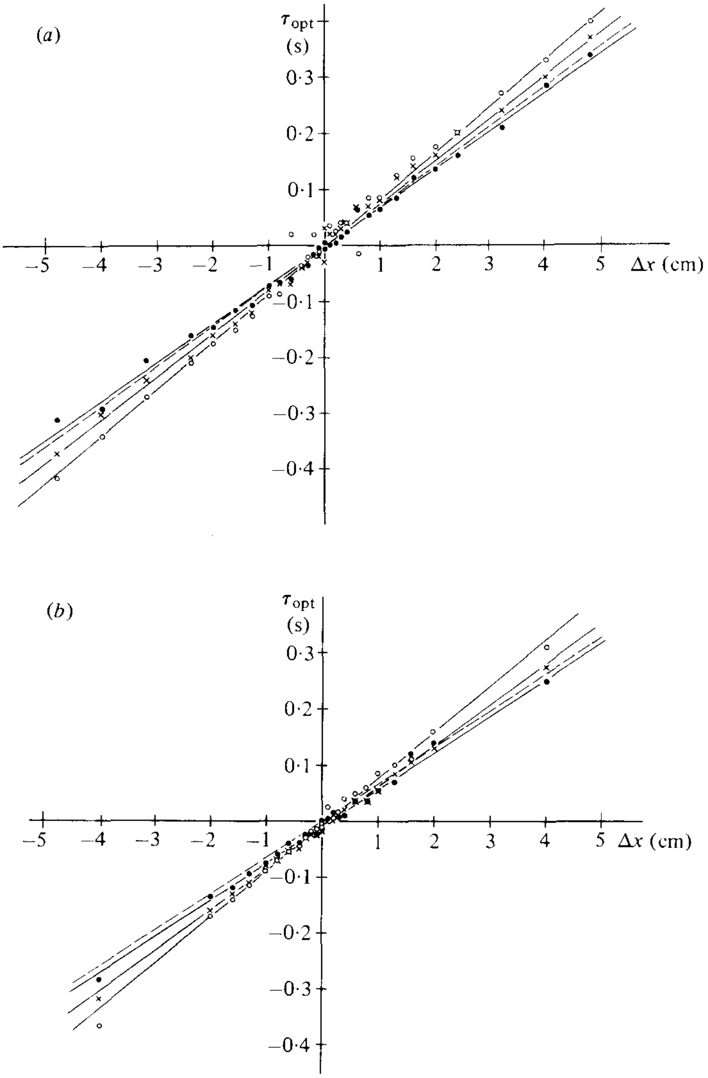

FIGURE 24(*a*, *b*). For the caption see the next page.

tends to increase with y/h. In order to examine the spanwise spatial structure more quantitatively, we analyse here the spatial structures of $\langle\hat{u}\rangle_e(y, \Delta z)$ and $\langle\hat{u}\rangle_s(y, \Delta z)$, where $\Delta x \equiv 0$, $y \equiv y_0 \equiv y_1$, $z_0 \equiv 0$ and $z_1 \equiv \Delta z \equiv z$, by making use of the conditional average of (9) and (10).

Figure 27 shows an example of the conditionally averaged spanwise structure $\langle\hat{u}\rangle(z)$ obtained at $Re = 1{\cdot}1 \times 10^4$ (case R-1), in which $\langle\hat{u}\rangle_e(y, z)$ of the ejections is normalized by $\langle\hat{u}\rangle_e(y, z = 0)$. Evidently, the spanwise spatial scale increases with an increase of y/h. However, the existence of the stable cellular secondary flow shown in figure 1 is not clear, because $\langle\hat{u}\rangle(z)$ decays fairly rapidly up to $z/h = 2$.

Some periodicity of $\langle\hat{u}\rangle(z)$ is recognized with certainty near the wall, and it perhaps corresponds to the high- and low-speed streaks observed visually. However, its

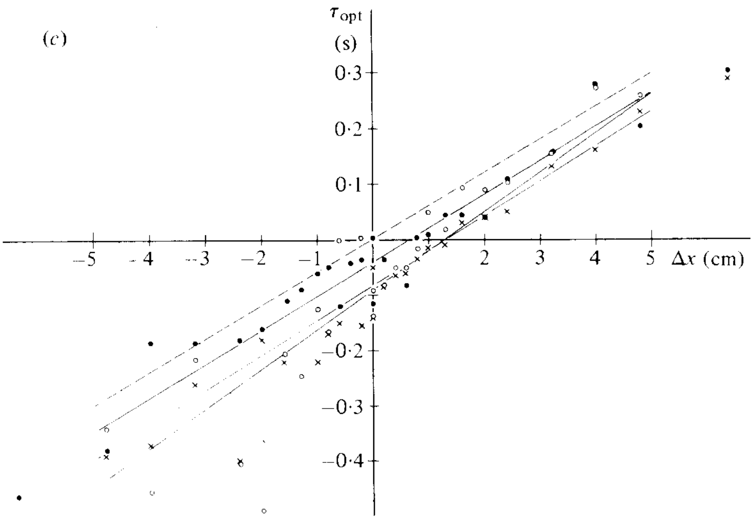

FIGURE 24. Optimum delay time τ_{opt} of $\langle\hat{u}\rangle$ *versus* the separation Δx. (*a*) y = 0·4 cm (y/h = 0·05, y^+ = 38); ——, convection velocity U_c; ○, $\langle\hat{u}\rangle_e$, 12·0 cm s^{-1}; ●, $\langle\hat{u}\rangle_s$, 14·6 cm s^{-1}; ×, C_{uu}, 13·2 cm s^{-1}. – – –, mean velocity U = 13·9 cm s^{-1}. (*b*) y = 0·7 cm y/h = 0·087, y^+ = 67); ——, convection velocity U_c; ○, $\langle\hat{u}\rangle_e$, 12·1 cm s^{-1}; ●, $\langle\hat{u}\rangle_s$, 15·2 cm s^{-1}; ×, C_{uu}, 13·6 cm s^{-1}. – – –, mean velocity U = 15·2 cm s^{-1}. (*c*) y = 1·3 cm (y/h = 0·16, y^+ = 125); ——, convection velocity; ○, $\langle\hat{u}\rangle_e$, 14·0 cm s^{-1}; ●, $\langle\hat{u}\rangle_s$, 16·1 cm s^{-1}; ×, C_{uu}, 15·9 cm s^{-1}; – – –, mean velocity U = 16·7 cm s^{-1}.

intensity is not so large, as compared with the results of Gupta *et al.* (1971) who analysed the spatial structure in the viscous sublayer by VITA-method using the signals of the ten-hot-wire rake. This difference can be explained in the following respects.

Now, assuming that the instantaneous pattern of the high-speed and low-speed streaks is approximately expressed by a cyclic function such as cos ($2\pi z/\lambda$) and that its amplitude or the detecting function of (9) or (10) is in proportion to the wavelength or the spacing λ, which is inferred from the results of Lee, Eckelman & Hanratty (1974), we can obtain as follows:

$$\frac{\langle u\rangle(z)}{\langle u\rangle(z=0)} = \frac{1}{\bar{\lambda}}\int_0^\infty \lambda\cos(2\pi z/\lambda)\,P(\lambda)\,d\lambda, \tag{25}$$

where $P(\lambda)$ is the probability of the occurrence of λ. According to visual observations of Nakagawa & Nezu (1977*b*), $P(\lambda)$ is expressed by the log-normal distribution, that is

$$P(\lambda) = \frac{\log e}{(2\pi)^{\frac{1}{2}}\sigma_0\lambda}\exp\left\{-\frac{1}{2}\left(\frac{1}{\sigma_0}\log\frac{\lambda}{\lambda_0}\right)^2\right\}, \tag{26}$$

where $\sigma_0 \equiv (\log e)(\ln(1+\psi^2))^{\frac{1}{2}}, \quad \lambda_0 \equiv (1+\psi^2)^{-\frac{1}{2}}\bar{\lambda}.$

Some curves of (25) calculated by using (26) are shown *versus* $z/\bar{\lambda}$ in figure 28, as a parameter of $\psi \equiv \sigma/\bar{\lambda}$ (where $\bar{\lambda}$ is the mean value of λ, and σ is the standard deviation of λ). Even the curve of (25) with ψ = 0·5† evaluated from our visual data does not

---

† The value of the coefficient ψ of variation of the bursting period is nearly equal to 0·5–1·5, as mentioned in §4.1, refer to Nezu (1977*a*) and Nakagawa & Nezu (1978).

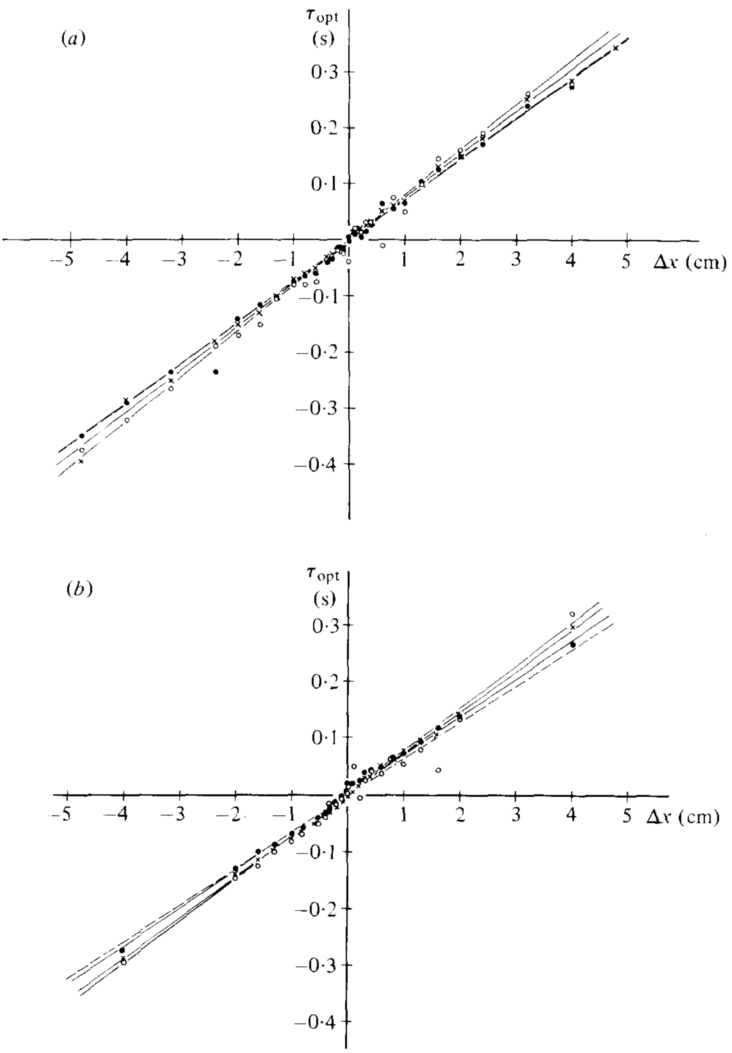

FIGURE 25 (*a*, *b*). For the caption see the next page.

show a strong periodicity any longer. This means that the high-speed and low-speed streaks are fairly smoothed even by the conditional average technique of two probe signals.

However, the effect of ψ on (25) is fairly small up to the first zero-cross point z_0. Then, by using $\psi = 0{\cdot}7$, we can obtain from (25) as follows:

$$\int_0^{z_0} \frac{\langle u \rangle (z)}{\langle u \rangle (z=0)}\, dz = 0{\cdot}16\bar{\lambda}. \tag{27}$$

Thus, the mean spacing $\bar{\lambda}$ can be defined tentatively so that the experimental values in figure 27 may satisfy (27). Such experimental values of $\langle \hat{u} \rangle$ are plotted in figure 28, *versus* $z/\bar{\lambda}$, i.e. the spanwise separation normalized by the mean spacing $\bar{\lambda}$ evaluated from (27). Figure 28 also shows the data of Nishioka, Iida & Shimizu (1977) who conducted the simultaneous measurements by three-hot-wire-rake detecting probe and

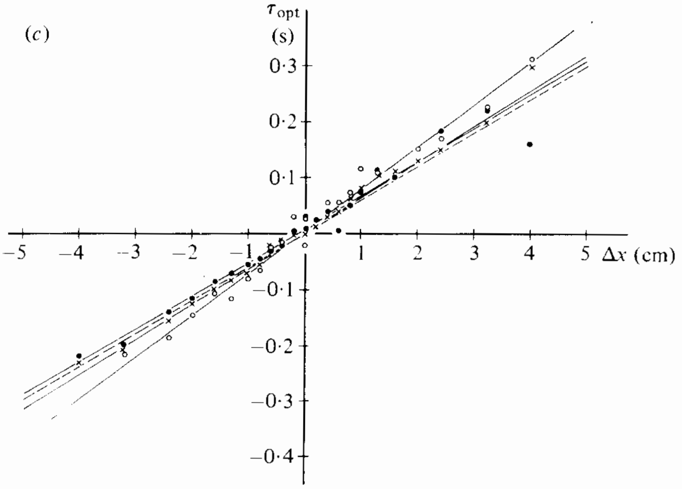

FIGURE 25. Optimum delay time τ_{opt} of $\langle \hat{v} \rangle$ versus the separation Δx. (*a*) $y = 0{\cdot}4$ cm: ——, convection velocity; ○, $\langle \hat{v} \rangle_e$, 12·4 cm s^{-1}; ● $\langle \hat{v} \rangle_s$, 13·9 cm s^{-1}, ×, C_{vv}, 13·1 cm s^{-1}. (*b*) $y = 0{\cdot}7$ cm: ——, convection velocity; ○, $\langle \hat{v} \rangle_e$, 13·3 cm s^{-1}; ●, $\langle \hat{v} \rangle_s$, 14·8 cm s^{-1}, ×, C_{vv}, 13·9 cm s^{-1}. (*c*) $y = 1{\cdot}3$ cm: ——, convection velocity; ○, $\langle \hat{v} \rangle_e$, 13·2 cm s^{-1}; ●, $\langle \hat{v} \rangle_s$, 16·8 cm s^{-1}; ×, C_{vv}, 15·6 cm s^{-1}. – – –, mean velocity (see figure 24).

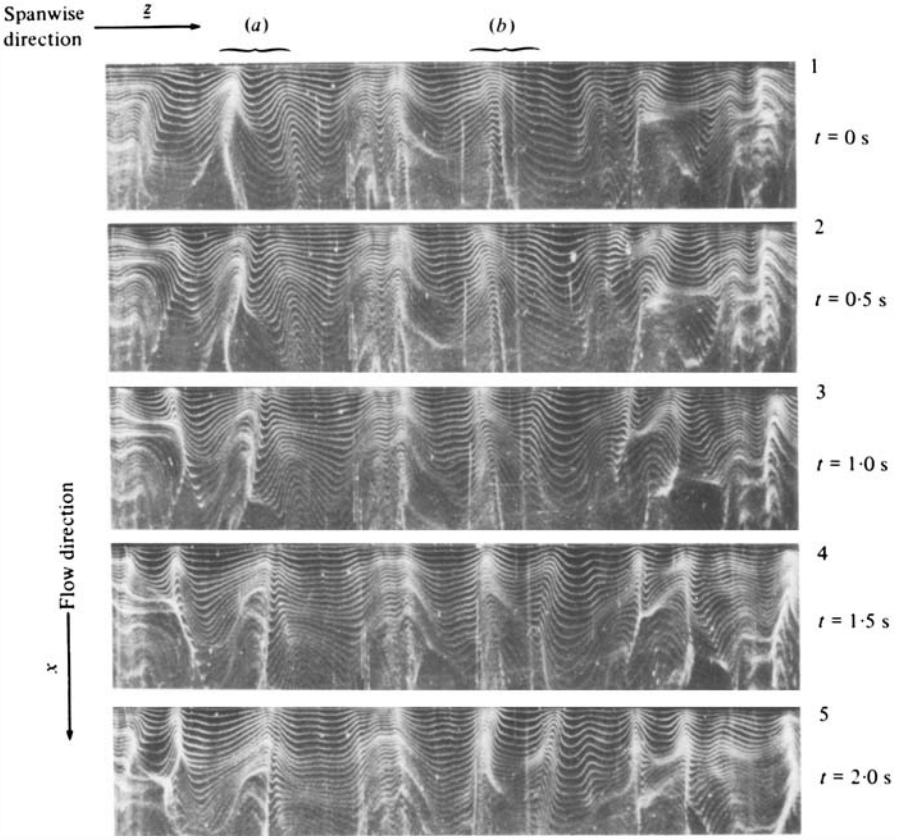

FIGURE 26. Streaky structure in the viscous sublayer ($y^+ = 4{\cdot}4$) visualized by means of hydrogen-bubble tracer (Nakagawa & Nezu 1977*b*). The sequence of five motion film frames, separated in time by 0·5 s, illustrate a coalescence (shown by (*a*)) and a division (shown by (*b*)) of the streaks. $R_e = 2700$, $R_* = 163$.

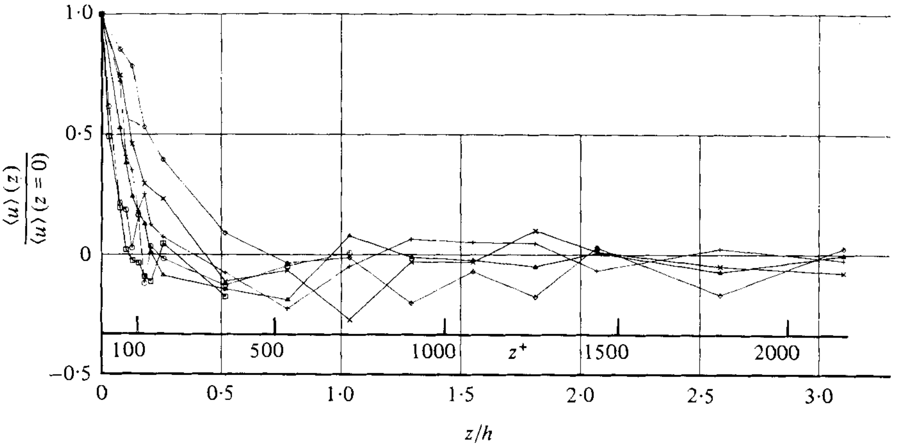

FIGURE 27. Spanwise spatial correlations $\langle u\rangle(z)/\langle u\rangle$ $(z=0)$ of the ejections for $\tau = 0$, as a function of y/h, case R-1. $(y/h, y^+)$: □, (0·052, 36); ○, (0·091, 63); △, (0·168, 117); +, (0·310, 216); ×, (0·517, 360); ◇, (0·776, 540).

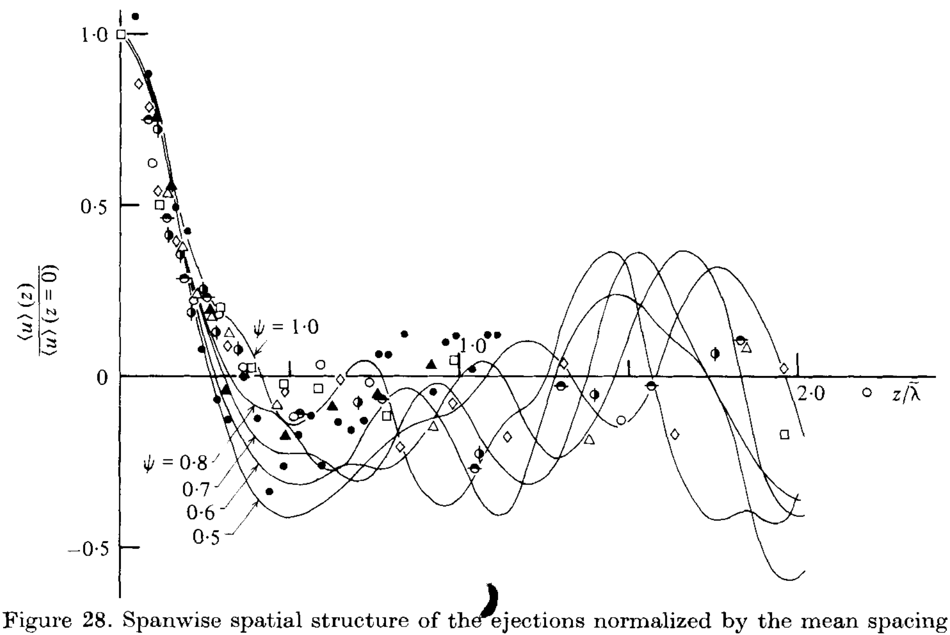

Figure 28. Spanwise spatial structure of the ejections normalized by the mean spacing $\bar{\lambda}$. The present data $(R_* = 696)$: □, $y^+ = 36$; ○, $y^+ = 63$; △, $y^+ = 117$; ◐, $y^+ = 216$; ⊖, $y^+ = 360$; ◇, $y^+ = 540$. ●, $y^+ = 10$, Nishioka *et al.* (1977), $R_* = 150$; ▲, spanwise correlation of $(\partial u/\partial y)|_{y=0}$, Kreplin & Eckelmann (1979), $R_* = 200$. ——, calculated curves of equation (25) with $\psi = 0·5$ to $1·0$.

single sampling probe in an air pipe, and the recent data of Kreplin & Eckelmann (1979) who measured the spanwise correlations of the velocity gradient at the wall by flush-sensor hot-films in an oil channel. A good agreement between the experimental and calculated values is recognized up to $z/\bar{\lambda} \simeq 0·5$, i.e. the spacing between the high-speed and low-speed streaks. Therefore, the present evaluation method of $\bar{\lambda}$ seems to be reasonable. Also, these spatial features are true for the sweeps.

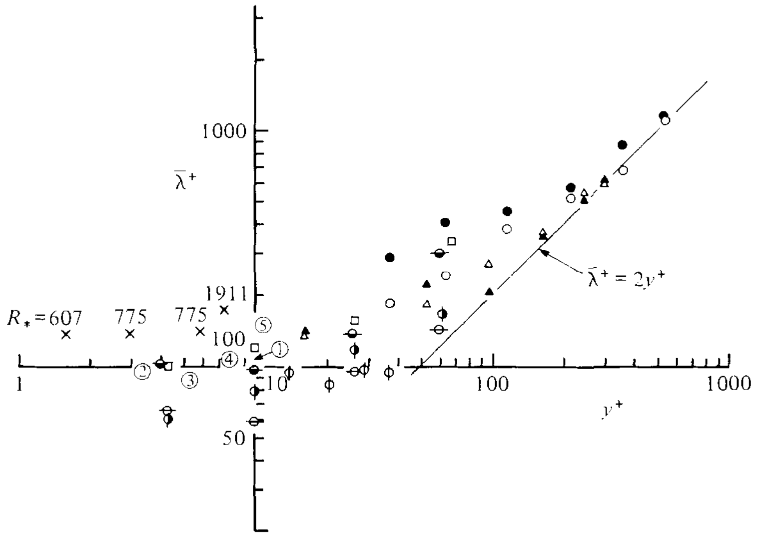

FIGURE 29. Variation of the mean spacing $\bar{\lambda}^+$ between the high-speed and low-speed streaks, as a function of y^+. The present data (open channel, hot film): △, $\bar{\lambda}_e$, $R_* = 318$; ▲, $\bar{\lambda}_s$, $R_* = 318$; ○, $\bar{\lambda}_e$, $R_* = 696$; ●, $\bar{\lambda}_s$, $R_* = 696$. Nakagawa & Nezu (1977*b*) (open channel, visual data): ϕ, $R_* = 102$; ⊖, $R_* = 113$; ◐, $R_* = 163$; ⊖, $R_* = 248$; □, $R_* = 378$. Nishioka *et al.* (1977) (pipe, hot wire): ①, $R_* = 150$. Gupta *et al.* (1971) (boundary layer, hot wire): ②, $R_* = 871$; ③, $R_* = 1254$; ④, $R_* = 1688$; ⑤, $R_* = 2160$. Morrison *et al.* (1971) (pipe, hot wire): ×, spectral method.

Figure 29 shows the mean spacing $\bar{\lambda}^+$ versus y^+ for the ejections and sweeps, together with the previous anemometry and visual results. $\bar{\lambda}^+$ is nearly equal to constant, i.e. $\bar{\lambda}^+ \simeq 100$, in the buffer layer ($y^+ \leqslant 30$). It is surprising that Morrison, Bullock & Kronauer (1971) could obtain the streaky spacing $\bar{\lambda}^+ = 135$ in the viscous sublayer ($y^+ \leqslant 5$) even by the long-time averaging spectral method, in contrast with the remarks of Gupta *et al* (1971). Also, Lee *et al.* (1974) and Kreplin & Eckelmann (1979) could obtain the streaky spacing $\bar{\lambda}^+ \simeq 100$ of the velocity gradient at the wall by the long-time averaging correlation method. These results indicate that the streaky structure of the viscous sublayer can be detected even by the conventional long-time averaging methods. In other words, this suggests that the viscous sublayer may be regarded as a stable 'footprint' of the bursting motions.

The mean spacing $\bar{\lambda}^+$ increases gradually in the region of $y^+ \geqslant 30$, and then approaches a relation of $\bar{\lambda}^+ = 2y^+$ in the outer region. This suggests that there may exist an interaction or pairing (coalescence) between the high-speed and low-speed streaks and that its spacing on the free surface becomes nearly equal to $2h$, as shown in figure 1.

As seen in the successive pictures of figure 26, the wall streaks coalesce, (*a*), and divide, (*b*), each other repeatedly in space and time, and consequently their mean spacing $\bar{\lambda}^+$ is kept to be constant. The coalescence or pairing mechanism is recognized in common in the coherent turbulent structures such as mixing layer, boundary layer, jets and wakes (e.g. see Laufer 1975). On the other hand, the division or break-up mechanism is caused by an inrush motion of accelerated fluid, i.e. sweeps, in the

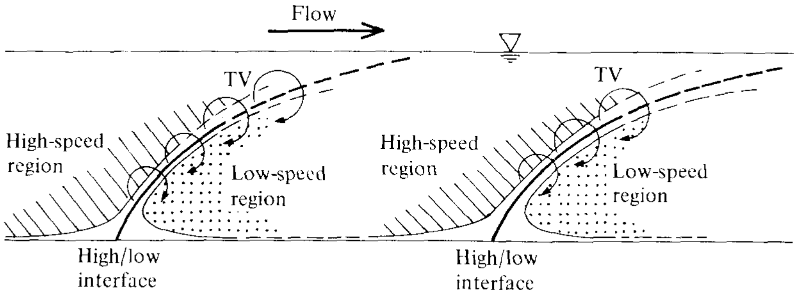

FIGURE 30. A model of high-speed and low-speed regions in an channel flow.

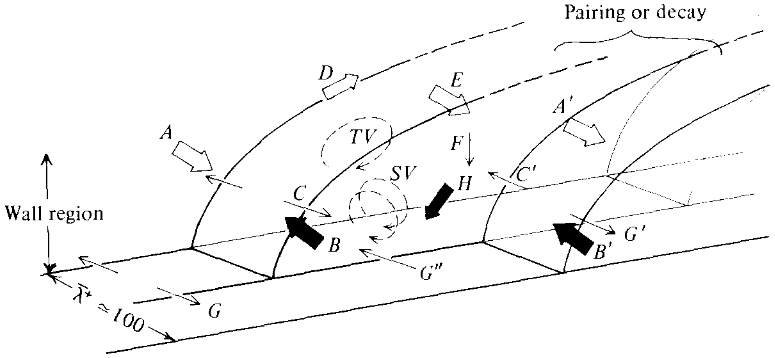

FIGURE 31. A conceptual model of the bursting motions in an open-channel flow. ⇨, high-speed fluid ($u > 0$); ➡, low-speed fluid ($u < 0$). *SV*, streamwise vortex: *TV*, transverse vortex.

Offen–Kline model (1975). Consequently, the coalescence of the streaky structure seems to prevail over its division in the region of $y^+ \geqslant 30$, because the inrush motion becomes weaker farther from the wall (Grass 1971; Nakagawa & Nezu 1977*a*).

5. Qualitative model of the bursting phenomenon

A phenomenological model to describe the space–time structures of the bursting phenomenon is proposed here on the basis of the above results, and its simplified model is shown in figure 30. It can be judged from the present study and other visual studies that there certainly exist a high-speed region and a low-speed region alternately in an open-channel flow, although the velocity difference between the two regions may be not so large. A high-speed region probably moves toward the wall with a small angle and comes into a low-speed region, as seen in figure 23(*a*). Consequently, an interface or a high-speed front is formed between the high-speed and low-speed regions (see figure 30), although its sharp line of demarcation does not exist. An interaction between the high-speed and low-speed fluids is considered to form a coherent structure with ejection and sweep motions. A sweep motion shown by *A* in figure 31, which is described in the convected view with its coherent structure, appears remarkably at a place immediately upstream of the high/low interface and far from the wall. Then an ejection motion, shown by *B* in figure 31, occurs remarkably at a place immediately downstream from the interface. It is one of the most characteristic points that the transition from the high-speed region on the upstream side to the low-speed region on the downstream side occurs more rapidly than the opposite transition, as shown in figure 30. Of course, this high/low interface has a three-dimensional structure, and moreover, it appears at random in space and time. However, the coherent structure near its interface is convected downstream with a longer lifetime at least than the bursting passing-period, namely in the frozen-turbulence-like manner. Thus, in the Eulerian observation of its coherent structure, a cyclic variation (slow deceleration of u) → (ejection motion) → (rapid transition to the sweep motion, i.e. rapid acceleration of u) → (slow deceleration of u), can be recognized on an average.

We must consider the coherent bursting motions in three-dimensional aspects. According to the present anemometry study and many other visual studies, the spanwise structure consists of high-speed and low-speed streaks whose spacing λ^+ is nearly equal to 100 in the wall region, but tends to increase gradually with y/h outside the wall region. Figure 31 shows a conceptual model of the bursting motions, in which the white and the black arrows denote the high-speed and low-speed fluids, respectively, in regard to the convected view with the coherent structure. Since the high/low interface is fairly inclined downstream toward the wall, a high-speed fluid (A) (i.e. a sweep motion) penetrates toward the wall and undergoes a complicated interaction with a low-speed fluid (B) (i.e. an ejection motion). As a result of this interaction, (A) and (B) are entangled with each other and combined into a spanwise outflow (C) and a high-speed fluid (D) travelling along the interface which corresponds to an outward-interaction motion (i.e. $u > 0$ and $v > 0$), due to a condition of continuity. Of course, this interaction itself corresponds to the mechanism of turbulence production. (D) develops in the outer layer and then its part (E) returns toward the wall. Next, (E) and a spanwise inflow (C') from the neighbouring bursting motion are combined into a downflow (F) and a new high-speed fluid (A'). (F) comes into the low-speed region and thus changes into a low-speed fluid (H), which may in part correspond to an inward-interaction motion (i.e. $u < 0$ and $v < 0$). On addition of a spanwise inflow (G'') caused by a consequence of continuity of (C), the low-speed fluid (H) develops in the wall region due to a strong velocity shear stress, and then it is supplied to the ejection motion (B).

Consequently, such a sequence of these fluid motions forms and keeps a coherent structure over a longer convection distance than several times the flow depth. In this coherent structure, (D) and (E) form a transverse vortex near the high/low interface. It may be truly said that (D) and (E) are formed by a transverse vortex caused by a Helmholtz-type interaction between the high-speed and low-speed regions (see figure 30). An inflow and outflow, e.g. (G'') and (C), between the neighbouring spanwise structures also form a streamwise vortex, as shown in figure 31. Thus, the streamwise vortices appear more markedly closer to the wall, while the transverse vortices appear more markedly farther from the wall, which is in good agreement with the visual observation by Nychas *et al.* (1973). Indeed, a composite model of the streamwise and transverse vortices makes up a horseshoe vortex which was first proposed by Theodorsen (1955) and was then adopted as an origin of Black's model (1968) and our Π-eddy model (Nakagawa & Nezu 1974). It is strongly suggested from the present study that such horseshoe vortices may develop up to the outside of the wall region and then coalesce. However, it has to be emphasized here that the present model of figure 31 has been proposed on a basis of the available fragmentary information of the conditionally ensemble-averaged velocity patterns $\langle u \rangle$ and $\langle v \rangle$. Thus, it is as yet unknown whether a horseshoe vortex itself exists or not as a real-time coherent structure, as pointed out by Praturi & Brodkey (1978).

From the above consideration, the present model can explain satisfactorily some of the most essential characteristics of the bursting motions obtained from the present anemometry study. The present model is in many respects consistent with some coherent models in a boundary layer which were proposed by Falco (1977), Brown & Thomas (1977) and Praturi & Brodkey (1978). The most similar and essential feature is that the high/low interface plays a very important role in these models, and that the coherent vortices are generated close to its interface.

Lastly, we should consider how the coherent structure of figure 31 will change in a larger Reynolds-number flow, although the present experiments have been carried out at relatively low Reynolds numbers. In this respect, a double-structure model proposed by Falco (1977) and Nakagawa & Nezu (1977*b*, 1978) may be still attractive. Its model consists of a larger-scale eddy which scales with the outer parameter h and a smaller-scale eddy which scales with the inner parameter ν/U_*, and these two eddies coexist consistently as if a smaller-scale eddy rides on a larger-scale eddy, between which there exists an energy cascade process. According to Falco's model (1977), a smaller-scale and larger-scale eddies correspond to a bursting and bulge motions, respectively, in a boundary layer, which were surely visualized clearly by Falco (1977, see his figure 1). In a smooth open channel, however, no bulge motion exists, nor is a strong cellular secondary flow shown in figure 1 recognized, as mentioned earlier.

Therefore, we cannot conclude clearly that the present model of figure 31 represents only a smaller-scale eddy or a wall streaky structure which may be, in practice, very little contributive to an open-channel flow, when the Reynolds number $R_* \equiv h/(\nu/U_*)$ is sufficiently large. So, it is very important in a basic and applied hydraulics to investigate further the space-time structure of the bursting phenomenon over a rough or wavy beds which probably generate a strong cellular secondary flow. For example, Nakagawa & Nezu (1980) have reported some interrelation between the bursting phenomenon and the cellular secondary flow in an open channel.

6. Conclusions

The present study has investigated the structure of space–time correlations of bursting motions, such as ejections and sweeps in an open-channel flow, by a new conditional sampling analysis of the instantaneous velocity and Reynolds-stress signals measured simultaneously by two dual-sensor hot-film probes. One probe was fixed near the edge of the buffer layer and used as a detecting probe of the bursting motions. The other probe was moved in the streamwise, vertical and spanwise directions. The main findings obtained from the above are as follows:

(1) The spatial and time scales of the streamwise turbulent velocity component are larger than those of the vertical velocity component.

(2) The spatial and time scales of the sweep motion are larger than those of the ejection motion.

(3) The spatial scale of the ejection motion extends more widely downstream than upstream, and vice versa for the sweep motion.

(4) The bursting motion is a kind of large-scale eddy structure, and its coherent structure is fairly inclined downstream toward the wall. It is convected downstream

with a longer lifetime than the bursting passing-period, namely in the frozen-turbulence-like manner.

(5) Although the spanwise spacing between the high- and low-speed streaks is nearly constant in the buffer layer, it increases gradually with an increase of the vertical position in the outer region.

Next, a qualitative model has been proposed with attempted to explain the space–time structures of the bursting phenomenon, on the basis of the above fragmentary information and other visual observations. The present model could explain satisfactorily some of the most essential characteristics of the bursting motions. However, a great part of the cause-and-effect relationship of bursting phenomenon or coherent vortex motions is yet unknown, even qualitatively. Above all, it is quite unknown why the high- and low-speed regions exist alternately in both the streamwise and spanwise directions in a turbulent shear flow. Hence, a more detailed experimental investigation of the bursting phenomenon by simultaneous anemometry and visual measurements is necessary under various hydraulic conditions.

The authors wish to thank Mr N. Matsumoto, an engineer of Ministry of Construction, for his experimental and analytical aid in this work. Also, we should like to thank some referees of this journal for their relevant advice.

REFERENCES

BARK, F. H. 1975 *J. Fluid Mech.* **70**, 229.

BLACK, T. J. 1968 *A.I.A.A. Paper* no. 68–42.

BLACKWELDER, R. F. & KAPLAN, R. E. 1976 *J. Fluid Mech.* **76**, 89.

BLACKWELDER, R. F. & KOVASZNAY, L. S. G. 1972 *Phys. Fluids* **15**, 1545.

BREMHORST, K. & WALKER, T. B. 1973 *J. Fluid Mech.* **61**, 173.

BRODKEY, R. S., WALLACE, J. M. & ECKELMANN, H. 1974 *J. Fluid Mech.* **63**, 209.

BROWN, G. L. & THOMAS, A. S. W. 1977 *Phys. Fluids* **20**, S243.

CORINO, E. R. & BRODKEY, R. S. 1969 *J. Fluid Mech.* **37**, 1.

ECKELMANN, H. 1974 *J. Fluid Mech.* **65**, 439.

EINSTEIN, H. A. & LI, H. 1956 *Proc. A.S.C.E.* EM-2, pp. 1–27.

FALCO, R. E. 1977 *Phys. Fluids* **20**, S124.

FAVRE, A. J. 1965 *J. Appl. Mech.* **32**, 241.

GRASS, A. J. 1971 *J. Fluid Mech.* **50**, 233.

GUPTA, A. K., LAUFER, J. & KAPLAN, R. E. 1971 *J. Fluid Mech.* **50**, 493.

HINZE, J. O. 1975 *Turbulence* (2nd edn), pp. 586–770. McGraw-Hill.

JACKSON, R. E. 1976 *J. Fluid Mech.* **77**, 531.

KIM, H. T., KLINE, S. J. & REYNOLDS, W. C. 1971 *J. Fluid Mech.* **50**, 133.

KINOSHITA, R. 1967 *Photographic Surveying* **6**, 1 (in Japanese).

KLINE, S. J., REYNOLDS, W. C., SCHRAUB, R. A. & RUNSTADLER, P. W. 1967 *J. Fluid Mech.* **30**, 741.

KOVASZNAY, L. S. G., KIBENS, V. & BLACKWELDER, R. F. 1970 *J. Fluid Mech.* **41**, 283.

KREPLIN, H. P. & ECKELMANN, H. 1979 *J. Fluid Mech.* **95**, 305.

LANDAHL, M. T. 1967 *J. Fluid Mech.* **29**, 441.

LANDAHL, M. T. 1977 *Phys. Fluids Suppl.* **20**, 55. See also *Hydraulic Problems Solved by Stochastic Methods* (ed. P. Hjorth, L. Jönsson & P. Larsen), *2nd Int. Symp. Stochastic Hydraulics*, no. 1, pp. 1–22, 1977.

LAUFER, J. 1954 *N.A.C.A.* TR-1174.

LAUFER, J. 1975 *Ann. Rev. Fluid Mech.* **7**, 307.

LAUFER, J. & NARAYANAN, M. A. B. 1971 *Phys. Fluids* **14**, 182.

LEE, M. K., ECKELMAN, L. D. & HANRATTY, T. J. 1974 *J. Fluid Mech.* **66**, 17.

LU, S. S. & WILLMARTH, W. W. 1973 *J. Fluid Mech.* **60**, 481.

MORRISON, W. R. B., BULLOCK, K. J. & KRONAUER, R. E. 1971 *J. Fluid Mech.* **47**, 639.

MÜLLER, A. 1977 *Hydraulic Problems Solved by Stochastic Methods* (ed. P. Hjorth, L. Jönsson & P. Larsen), *2nd Int. Symp. Stochastic Hydraulics*, no. 3, pp. 1–22.

NAKAGAWA, H. & NEZU, I. 1974 *Proc. Japan Soc. Civil Eng.* **231**, 61–70.

NAKAGAWA, H. & NEZU, I. 1977*a* *J. Fluid Mech.* **80**, 99.

NAKAGAWA, H. & NEZU, I. 1977*b* *5th Symp. Flow Visualization, ISAS, Univ. of Tokyo*, no. 5, pp. 47–50 (in Japanese).

NAKAGAWA, H. & NEZU, I. 1978 *Memoirs, Fac. Engng Kyoto Univ.* **40**, 213.

NAKAGAWA, H. & NEZU, I. 1979 *Memoirs, Fac. Engng Kyoto Univ.* **41**, 240.

NAKAGAWA, H. & NEZU, I. 1980 *ICHMT/IUTAM Symp. Heat and Mass Transfer and Structure of Turbulence, Dubrovnik.* Hemisphere.

NAKAGAWA, H., NEZU, I. & MATSUMOTO, N. 1980 *Memoirs, Fac. Engng Kyoto Univ.* **42**, 85.

NEZU, I. 1977*a* Turbulent structure in open-channel flows. Ph.D. thesis, Kyoto University.

NEZU, I. 1977*b* *Proc. Japan Soc. Civil Eng.* **261**, 67–76 (in Japanese).

NEZU, I., NAKAGAWA, H. & TOMINAGA, A. 1980 *Ann. Meeting, Japan Soc. Civil Eng.* no. II, p. 210 (in Japanese).

NEZU, I. & NAKAGAWA, H. 1981 *25th Japanese Conf. on Hydraulics.* (To be published.)

NEZU, I., NAKAGAWA, H. & TOMINAGA, A. 1981 *Proc. Japan Soc. Civil Eng.* (To appear.)

NISHIOKA, M., IIDA, S. & SHIMIZU, K. 1977 *9th Symp. Turbulence, ISAS, Univ. of Tokyo*, pp. 129–136 (in Japanese).

NYCHAS, S. G., HERSHEY, H. C. & BRODKEY, R. S. 1973 *J. Fluid Mech.* **61**, 513.

OFFEN, G. R. & KLINE, S. J. 1975 *J. Fluid Mech.* **70**, 209.

PRATURI, A. K. & BRODKEY, R. S. 1978 *J. Fluid Mech.* **89**, 251.

ROTTA, J. C. 1972 *Turbulente Strömungen*, cha. 3. B. G. Teubner.

SABOT, J. & COMTE-BELLOT, G. 1976 *J. Fluid Mech.* **74**, 767.

THEODORSEN, T. 1955 *50 Jahre Grenzschichtforschung* (ed. H. Görtler & W. Tollmien), pp. 55–62. Frier.

WALLACE, J. M., BRODKEY, R. S. & ECKELMANN, H. 1977 *J. Fluid Mech.* **83**, 673.

WILLMARTH, W. W. 1975 *Adv. Appl. Mech.* **15**, 159.